

# 2D Particle-in-cell simulations of charged particle dynamics in geometrically asymmetric low pressure capacitive RF plasmas

Li Wang<sup>1,2</sup>, Peter Hartmann<sup>3</sup>, Zoltán Donkó<sup>3</sup>, Yuan-Hong Song<sup>1,\*</sup>  
and Julian Schulze<sup>1,2</sup>

<sup>1</sup> Key Laboratory of Materials Modification by Laser, Ion, and Electron Beams (Ministry of Education), School of Physics, Dalian University of Technology, Dalian 116024, People's Republic of China

<sup>2</sup> Department of Electrical Engineering and Information Science, Ruhr-University Bochum, D-44780, Bochum, Germany

<sup>3</sup> Institute for Solid State Physics and Optics, Wigner Research Centre for Physics, H-1121 Budapest, Konkoly-Thege Miklós str. 29-33, Hungary

E-mail: [songyh@dlut.edu.cn](mailto:songyh@dlut.edu.cn)

Received 31 October 2020, revised 23 February 2021

Accepted for publication 25 March 2021

Published 27 August 2021



CrossMark

## Abstract

Understanding the spatio-temporal dynamics of charged particles in low pressure radio frequency capacitively coupled plasmas (CCP) is the basis for knowledge based process development in these plasma sources. Due to the importance of kinetic non-local effects the particle in cell/Monte Carlo collision (PIC/MCC) simulation became the primary modeling approach. However, due to computational limitations most previous PIC/MCC simulations were restricted to spatial resolution in one dimension. Additionally, most previous studies were based on oversimplified treatments of plasma-surface interactions. Overcoming these problems could clearly lead to a more realistic description of the physics of these plasma sources. In this work, the effects of the reactor geometry in combination with realistic heavy particle and electron induced secondary electron emission coefficients (SEEC) on the charged particle dynamics are revealed by GPU based 2D3V PIC/MCC simulations of argon discharges operated at 0.5 Pa and at a high voltage amplitude of 1000 V. The geometrical reactor asymmetry as well as the SEECs are found to affect the power absorption dynamics and distribution functions of electrons and ions strongly by determining the sheath voltages and widths adjacent to powered and grounded surface elements as well as via the self-excitation of the plasma series resonance. It is noticed that secondary electrons play important roles even at low pressures. Electron induced secondary electrons ( $\delta$ -electrons) are found to cause up to half of the total ionization, while heavy particle induced secondary electrons ( $\gamma$ -electrons) do not cause much ionization directly, but induce most of the  $\delta$ -electron emission from boundary surfaces. The fundamental insights obtained into the 2D-space



Original content from this work may be used under the terms of the [Creative Commons Attribution 4.0 licence](https://creativecommons.org/licenses/by/4.0/). Any further distribution of this work must maintain attribution to the author(s) and the title of the work, journal citation and DOI.

\* Author to whom any correspondence should be addressed.

resolved charged particle dynamics are used to understand the formation of energy distribution functions of electrons and ions for different reactor geometries and surface conditions.

**Keywords:** capacitively coupled plasmas, charged particle dynamics, realistic chamber geometries and secondary electron emission, formation of distribution functions

(Some figures may appear in colour only in the online journal)

## 1. Introduction

Due to their ability to generate large area and radially uniform plasmas above dielectric surfaces with controllable flux-energy and angular distribution functions of incident particle species, capacitively coupled radio frequency plasma (CCP) reactors are widely employed for material processing in micro-electronics technology [1–3]. For plasma etching realizing high aspect ratios (HAR) gets increasingly important and challenging as feature sizes continue to decrease. In order to realize high ion bombardment energies at the wafer (which are necessary to overcome the repelling effect of the deposited positive charge within the trenches [4–6]), a high driving voltage amplitude and a low neutral gas pressure are required to generate a collisionless high voltage sheath at the wafer.

In reality, most CCP reactors are geometrically asymmetric [7–12], i.e. the surface area of the grounded electrode is larger than that of the powered electrode. In such discharges, a negative DC self-bias is generated, which leads to the formation of a large high voltage sheath at the powered electrode. When positive ions fly through this sheath, they are accelerated and arrive at the wafer with a narrow angular distribution. As a consequence of the DC self bias the sheath voltages and, thus, the ion energy and angular distribution functions (IEDF & IADF) are different at the two electrodes. Due to the energy dependence of heavy particle induced secondary electron emission coefficients (SEECs) the probability of emitting a secondary electron per ion impact can also be drastically different at the two electrodes, even if both electrodes are made of the same material [13]. Moreover, the sheath expansion velocity that influences the generation of high frequency plasma series resonance (PSR) oscillations [14–17] is different at the two electrodes. Due to these effects, the electron energy distribution functions (EEDF) can be markedly different at the two electrodes in geometrically asymmetric CCPs. This, in turn, can lead to different electron induced SEECs at the two electrodes, since these emission coefficients depend on the incident electron energy [18, 19]. Such effects have not been investigated systematically before, since they require computationally demanding 2D kinetic simulations that include a realistic model for plasma-surface interactions.

Previous 1D PIC/MCC simulations have shown that plasma surface interactions indeed strongly affect the discharge characteristics under such conditions [20–22]. In particular, secondary electron (SE) emission from boundary surfaces can

drastically affect the plasma density and charged particle distribution functions [23–25]. Due to the lack of data for material specific and energy dependent surface coefficients, estimated and constant ion induced secondary electron ( $\gamma$ -electron) emission coefficients and electron reflection probabilities are usually included in the PIC/MCC simulations. Despite their simplifying assumptions these works demonstrated the important influence of the secondary electron emission coefficients on the discharge [26–29]. The ion induced SEEC was found to affect the discharge operation mode [30–33]. With a low  $\gamma$ -coefficient set at the surfaces, the discharge is usually found to be operated in the  $\alpha$ -mode [34–36], where electron power absorption and ionization during the sheath expansion phase dominate. By increasing the  $\gamma$ -coefficient, more ionization occurs inside the sheaths. This ionization mechanism becomes dominant at high pressures and driving voltage amplitudes, i.e. the plasma is operated in the  $\gamma$ -mode at much higher plasma density [37, 38]. In dual frequency discharges,  $\gamma$ -electrons were found to affect the quality of the separate control of the ion flux and mean ion energy at the electrodes [26, 39]. Moreover, Lafleur *et al* found that by operating the discharge between two electrodes with different materials, i.e. with different  $\gamma$ -coefficients at the powered and grounded electrode, a plasma asymmetry can be induced [40, 41].

Recently, more realistic heavy particle induced SEECs were included in PIC/MCC simulations of CCPs. In such models, the ion impact energy at the surface as well as the surface material were taken into account to determine the effective  $\gamma$ -coefficient [42–45] from the energy-dependent ion induced SEEC. By comparing the results of a realistic energy-dependent  $\gamma$ -electron emission model with simulation results obtained based on constant  $\gamma$ -coefficients, Daksha *et al* demonstrated that neglecting this energy-dependence in the simulations yields unrealistic results under many discharge conditions [42, 43]. The important influence of the surface material on the  $\gamma$ -coefficient is also pointed out in their work. They found that the surface properties can strongly change the operation mechanism of the discharge and can lead to different IEDFs at boundary surfaces [43, 44].

In addition to ion induced secondary electron emission, the effect of realistic electron induced SEECs has also been addressed in recent computational studies of CCPs [18, 46] by taking into account elastic electron reflection, inelastic backscattering and electron induced secondary electron ( $\delta$ -electron) emission. The coefficients of these processes

depend on the primary electron impact energy and angle at the surfaces as well as on the surface materials. By comparing the results of a realistic electron surface model and a simplified model, Horváth *et al* [18, 19] observed strongly different electron power absorption and ionization dynamics at low gas pressure. In such discharges, the  $\gamma$ -electrons emitted at one electrode can be accelerated to high energies in the local sheath, propagate through the bulk region collisionlessly and bombard the opposite electrode during the phase of local sheath collapse, i.e. they hit the electrodes with high energies. With a realistic  $\delta$ -electron emission coefficient set at the surfaces, such  $\gamma$ -electrons can induce a large number of  $\delta$ -electron emissions. After being accelerated by the expanding sheath, these  $\delta$ -electrons are found to greatly contribute to the ionization and to play a key role in the discharge.

Braginsky *et al* [47] also traced metastables and included secondary electron generation due to these particle species in a low pressure CCP operated in argon and driven at high voltage. They found that their contribution to secondary electron emission is low compared to that of argon ions. In the most recent 1D computational studies of CCPs [13, 48], a combined plasma-surface interaction model including realistic ion-, electron-, and atom-induced SEEs, has been implemented.

Another important issue for applications of CCPs is plasma uniformity [49–53]. In experiments [54–56] and simulations [57–61] several effects were found to affect the lateral uniformity of the discharge. Structured electrodes were found to influence the lateral plasma uniformity by changing the electron power absorption dynamics. For instance, the presence of trenches [62, 63] and wafer edges [64–67] can lead to curved sheaths and enhanced electric fields at edges, which affect the electron dynamics. A depleted plasma density along the radial direction was also found to be induced by the plasma transport towards the sidewall [67]. At high driving frequencies and large electrode diameters, the standing wave effect can cause lateral non-uniformity [68, 69]. At high plasma densities the skin effect can also be important [68, 70]. Such non-uniformity can lead to lateral changes of the electron power absorption dynamics and charged particle distributions across the electrode radius. Clearly, none of these effects can be addressed by 1D simulations, and investigation of some of these even requires electromagnetic simulations.

In this work, we investigate the 2D space resolved electron dynamics and charged particle distribution functions at boundary surfaces of CCPs by using GPU (Graphics Processing Unit) based 2D electrostatic PIC/MCC simulations as a function of the reactor symmetry and based on realistic ion and electron induced SEECs. In section 2, we describe the 2D PIC/MCC approach including the realistic SEE model. The results are presented in section 3, which consists of two parts: the effects of the geometric reactor asymmetry are studied in section 3.1, while the effects of individual surface coefficients on the charged particle dynamics are discussed in section 3.2. Concluding remarks are given in section 4.

## 2. 2D PIC/MCC simulation

We use a cylindrical 2D3V (two-dimensional in space and three-dimensional in velocity space) electrostatic PIC/MCC code to simulate plasmas in argon gas. As shown in figure 1, the plasma is operated between two electrodes, with the top electrode grounded (blue solid line) and the bottom electrode (red solid line) driven by the following voltage waveform:

$$V(t) = V_0 \cos(2\pi ft). \quad (1)$$

The driving voltage amplitude is  $V_0 = 1000$  V and the driving frequency is  $f = 13.56$  MHz. The diameter of the reactor is 24 cm and the gap distance between the plane parallel sections of both electrodes is 6.7 cm. Similar to experiments, a dielectric spacer (light blue solid line) with a length of 2.5 mm is used to separate the two electrodes. In experiments, this spacer can either be a dielectric or a thin gap, whose small width prevents gas breakdown inside this slit. In the simulations, the potential is assumed to drop linearly along the surface of the dielectric spacer. The plasma characteristics and electron dynamics are investigated in three different reactor geometries by setting the area ratio of the powered and grounded electrodes to different values. The reactor in figure 1(a) is geometrically symmetric, i.e. the area ratio is  $A_P/A_G = 1$ . In figures 1(b) and (c), asymmetric reactors with  $A_P/A_G = 0.7$  and  $0.46$  are shown. In order to observe the ionization dynamics near the center and near the sidewall separately and to understand the effects of the sidewall on the discharge, the reactor is divided into two regions of interest: the center region where the radial position is  $r \leq 6$  cm and the edge region with  $6 \text{ cm} < r < 12$  cm, as indicated by the green dashed lines in figure 1(a). While commercial CCP reactors typically have a more complicated geometry including side flanges and gas/plasma volumes in between the radial electrode edges and the sidewalls, the geometries shown in figure 1 represent a useful simplification, which limits the required computational effort, but still allows to draw important general conclusions with respect to the effects of the geometry of experimental systems [71–73] on the plasma characteristics.

The Poisson equation is solved in the 2D cylindrical system in the simulations assuming azimuthal symmetry. The microscopic coordinates of the charged particles, on the other hand, are stored and propagated in a 3D Cartesian coordinate system. In the latter, the electric field in the  $x$  and  $y$  directions is given as  $E_x = E_r \frac{x_i}{r_i}$  and  $E_y = E_r \frac{y_i}{r_i}$  for the calculation of the force acting on the particles, where  $x_i$  and  $y_i$  are the  $x$ - and  $y$ -coordinates of a specific particle, and  $r_i = \sqrt{x_i^2 + y_i^2}$  is its radial position. After pushing the particles in each time step, the radial and axial positions of each of the particles are checked to determine whether they reached the boundaries and interact with the surfaces. An isovolumetric grid is used in the simulations to determine the charged particle densities. This allows the number of superparticles in each grid cell to be balanced, providing

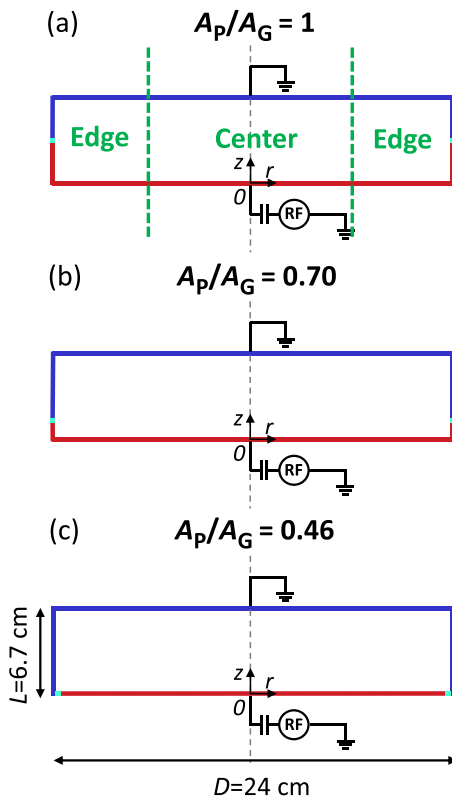


**Figure 1.** Reactor geometries investigated. The powered and grounded electrodes are indicated by the red and blue lines, respectively. The area ratios of the powered and grounded electrode are  $A_P/A_G = 1$  (a),  $A_P/A_G = 0.7$  (b), and  $A_P/A_G = 0.46$  (c), respectively. The vertical green dashed lines (shown only in (a)) separate the central plasma region ( $r \leq 6$  cm) and the edge region ( $6 \text{ cm} < r \leq 12$  cm).

a comparable level of statistical fluctuations in the grid cells near the center and near the sidewall. Before solving the Poisson equation, the charged particle densities are interpolated to an iso-distant grid. The potential is found as the linear superposition of two parts: the first part is the solution of the Poisson equation with the actual space charges and all boundary potentials set to 0 V; the second part is the potential obtained for a system in vacuum, i.e. only the boundary potentials are taken into account. The solution of the Poisson equation is found iteratively using the “red/black” parallel version of the successive over-relaxation method [74,75]. The electric fields are obtained from the potential by using the central difference scheme.

In our simulations, we trace electrons and  $\text{Ar}^+$  ions. The elastic scattering, excitation to 25 individual levels and ionization collisions between electrons and argon atoms; elastic scattering (including an isotropic and a backward (charge exchange) scattering channel), excitation to 3 individual levels and ionization collisions between  $\text{Ar}^+$  ions and argon atoms are included. The cross sections of these reactions can be found in references [13, 76–81]. More details concerning the collision processes in our code including the selection of colliding particles, the null collision method, and the treatment of particle velocities after a collision can be found in references [13, 82–84]

We use a realistic model to describe the interactions of electrons and ions with the  $\text{SiO}_2$  surfaces. The energy-dependent secondary electron yields for  $\text{Ar}^+$  ions for different surface materials have been analysed by Phelps and Petrović [85]. As we consider an oxidized surface, i.e.  $\text{SiO}_2$ , in the simulations, we use the SE yield function for ‘dirty metals’ provided in [85], which describes the SE yield due to ion bombardment at metal surfaces contaminated by oxygen, water, ambient gas, etc. Studies by Sobolewski [86] have shown that the ion induced SE yield at a  $\text{SiO}_2$  surface is similar to that at oxidized metal surfaces. This kind of treatment for the ion induced SEEC at  $\text{SiO}_2$  surfaces was also adopted in previous work [13]. For the electron-surface interactions, we assume the total SE flux due to electron bombardment at the surface to be composed of three parts: elastically reflected electrons, inelastically backscattered electrons, and true electron induced secondary emissions. The coefficients of these processes depend on the incident energy and angle of the primary electron and the surface properties. In our code, we adopt the model of Horvath *et al* to describe these interactions of electrons with  $\text{SiO}_2$  surfaces [13, 18, 19]. Figure 2(b) shows the electron induced SE yield of  $\text{SiO}_2$  as a function of the electron impact energy at normal incidence. The type of an electron (bulk-,  $\gamma$ - and  $\delta$ -electron) is defined, when the respective electron is generated. Electrons generated by electron impact ionization of neutrals are labeled ‘bulk electrons’. Electrons emitted from boundary surfaces due to ion impact are labeled ‘ $\gamma$ -electrons’, while those emitted from boundary surfaces due to electron impact are labeled ‘ $\delta$ -electrons’. Information on each type of electrons are stored in separate arrays. These labels are used for diagnostic purposes only and remain with the electron until it is absorbed at the surfaces. Otherwise, all electrons are treated in the same way in the simulation.

Based on the findings of Braginsky *et al* [47] as well as Phelps and Petrović [85] we neglect secondary electron emission due to argon metastables. In these previous works, secondary electron emission due to metastables was found to be low compared to that due to argon ions under conditions similar to those studied in this work. We note that the contribution of metastables to the generation of secondary electrons can vary under different discharge conditions [85]. The emission coefficients also strongly depend on the surface material and its conditions [87, 88].

The DC self-bias is adjusted self-consistently according to the difference of the time averaged positive and negative charged particle currents at the boundary surfaces in each RF cycle until a balance is achieved [89].

The gas temperature is fixed at 400 K in our simulations and the neutral gas pressure is 0.5 Pa. Under such conditions ( $f = 13.56$  MHz,  $V_0 = 1000$  V, 24 cm electrode diameter), electromagnetic effects can be ignored. In the simulations, 512 grid points in the axial direction and 512 to 1024 grid points in the radial direction are used to resolve the Debye-length. 8000 to 16000 time steps per RF period are used for the different simulation cases (corresponding to time resolutions of 4.6 ps–9.2 ps). This is required to trace the fastest secondary electrons accurately. By selecting the number of grid points and the time step in this way all stability criteria

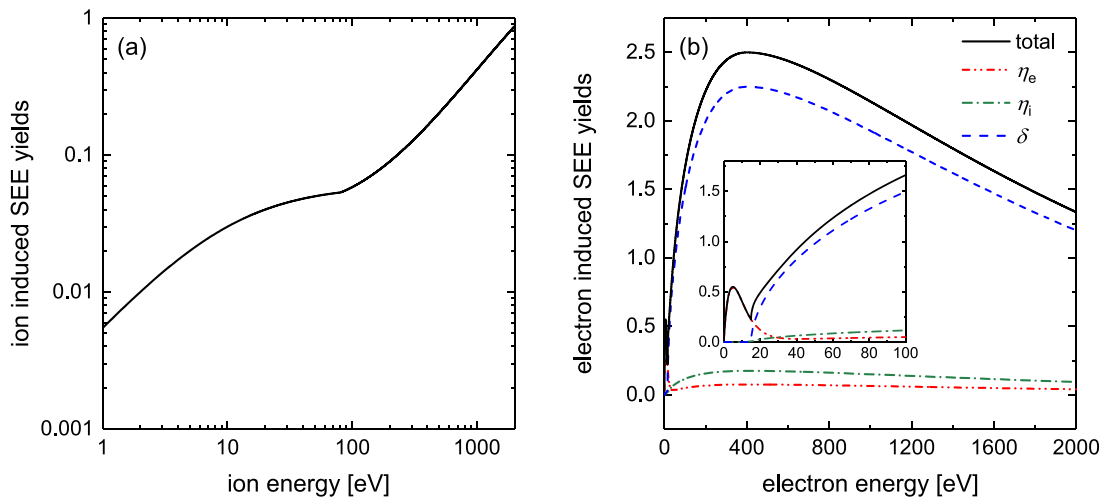


**Figure 2.** Impact energy dependent yields of surface processes included in the simulation:  $\text{Ar}^+$  induced secondary electron emission (SEE) for oxidized surfaces [85] (a); and electron induced electron emission processes (elastic reflection,  $\eta_e$ , inelastic reflection,  $\eta_i$ , and electron induced SEE at normal incidence,  $\delta$ ) for  $\text{SiO}_2$  surfaces [18] (b).

of the PIC/MCC scheme are fulfilled. Considering the large number of super particles ( $10^7 < N < 5 \times 10^7$ ) to be traced in 2D PIC/MCC simulations, we use graphics processing units (GPU) and the Nvidia compute unified device architecture (CUDA) programming language to perform the simulations. Each particle is assigned to an individual computational thread and all PIC/MCC steps and diagnostic routines are executed in parallel on the GPU. The simulations take around one week to converge. Compared to sequential CPU simulations the convergence of the GPU code is a factor of  $\sim 100$  faster. To achieve results with good signal to noise ratio data are acquired and averaged over 200 RF cycles in the simulation.

### 3. Results

#### 3.1. Effects of geometric reactor asymmetry on the charged particle dynamics

Figure 3 shows the space resolved and time averaged electron density for the three different reactor geometries shown in figure 1:  $A_P/A_G = 1$ , 0.7 and 0.46. In the simulation, a  $\gamma$ -coefficient according to figure 2(a) and a  $\delta$ -coefficient according to figure 2(b) are implemented at both the powered and the grounded electrode. The electron density is always found to be maximum at the reactor center and to decay towards the sidewalls at the low pressure of 0.5 Pa studied here. This is consistent with the results reported in reference [67], where the plasma density peak is found to move from the electrode edge to the center region as the gas pressure decreased. Due to the geometric asymmetry in the cases of  $A_P/A_G = 0.70$  and  $A_P/A_G = 0.46$ , a DC self-bias of  $-563$  V and  $-690$  V is generated, respectively. The maximum sheath widths at the powered electrode in these two cases are 1.04 cm and 1.27 cm, respectively, which are much larger than the sheath width in the symmetric case (0.70 cm). This causes the charged particle density profiles to shift towards the grounded electrode. Moreover, with the enhancement of the reactor asymmetry, the plasma density is reduced. A similar effect has previously been

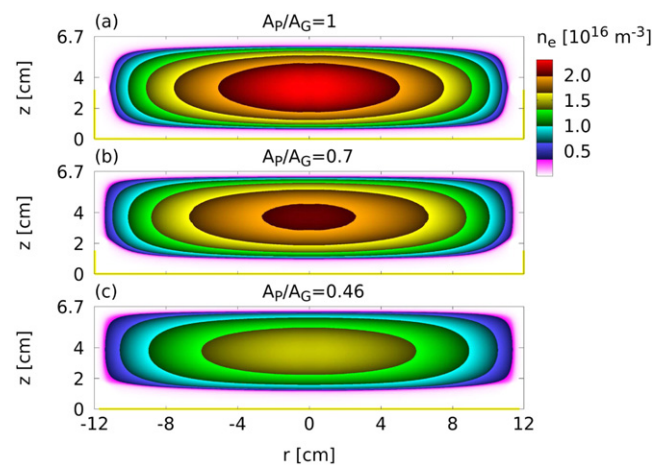


**Figure 3.** 2D spatial distributions of the time averaged electron densities for different reactor geometries. Discharge conditions: Ar, 0.5 Pa,  $f = 13.56$  MHz,  $V_0 = 1000$  V, 6.7 cm electrode gap, 24 cm electrode diameter, 400 K gas temperature,  $\text{SiO}_2$  surfaces.

observed experimentally by Hegemann *et al* [72, 73]. Here, the reduced density is mainly caused by the attenuated ionization adjacent to the larger grounded electrode during the sheath expansion phase. In the presence of the large DC self-bias, only a small sheath is formed at the larger grounded electrode, which leads to a depleted electron power absorption by sheath expansion heating at this electrode compared to the symmetric scenario.

In order to understand the effects of the sidewall on the electron heating, the spatio-temporal electron dynamics in the geometrically symmetric case is analyzed. Figure 4 shows the 2D (radially and axially) resolved spatial distribution of the total ionization rate at eight different times within one cycle of the cosine waveform RF excitation. Due to the high plasma density near the chamber center, the ionization is strong near  $r = 0$  and gradually decays along the radial direction at most times within the RF period. However, according to figures 4(b) and (f), another ionization peak is generated at the bottom

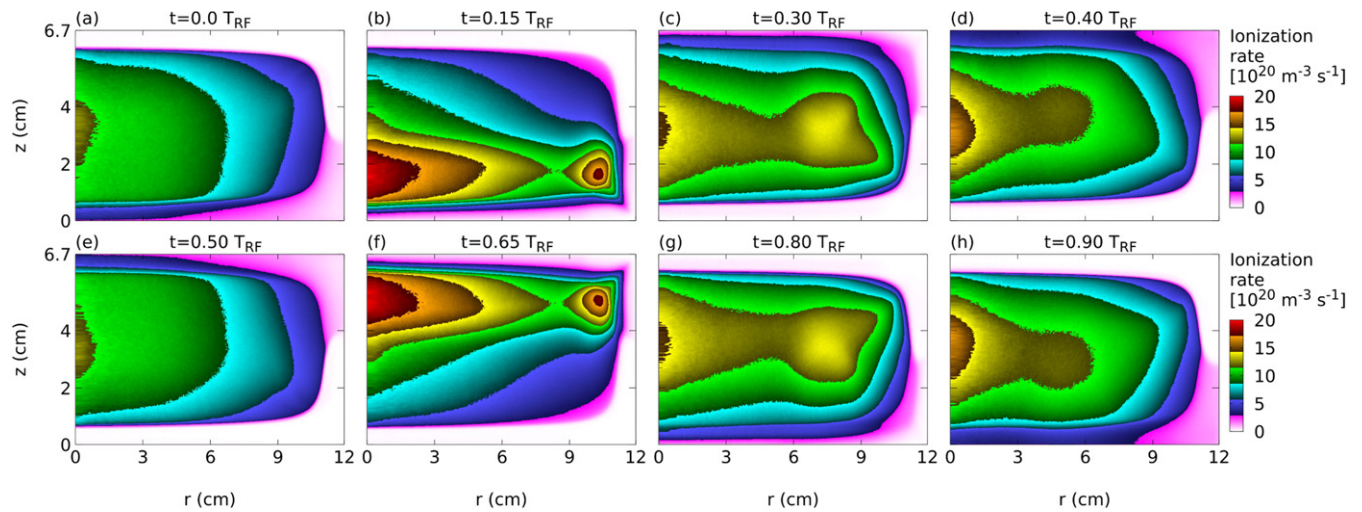


**Figure 4.** 2D spatial distribution of the total ionization rate at different times within one RF cycle in the geometrically symmetric reactor ( $A_P/A_G = 1$ ). Other discharge conditions are the same as in figure 3. Note that only the right half of the reactor is shown.

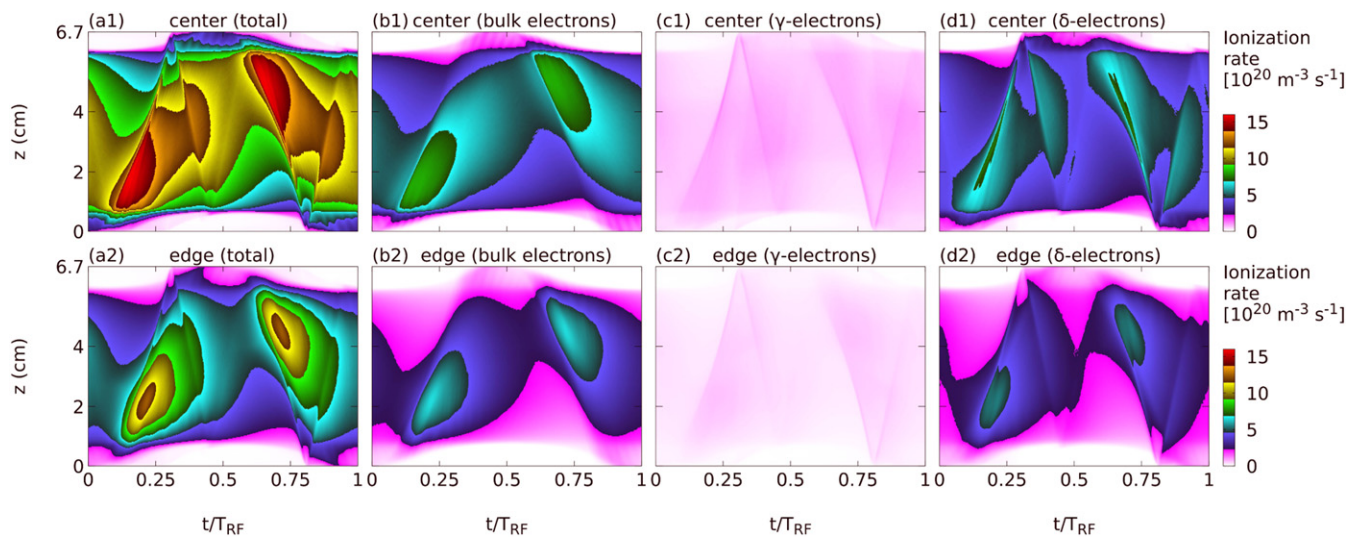


**Figure 5.** Axially and temporally resolved plots of the total ionization rate (first column), the ionization rate of bulk electrons (second column),  $\gamma$ -electrons (third column), and  $\delta$ -electrons (fourth column) in the geometrically symmetric scenario ( $A_P/A_G = 1$ ). Other discharge conditions are the same as in figure 3. The first row shows results obtained at the reactor center, and the second row shows the results obtained near the sidewall.

right corner at  $t = 0.15 T_{RF}$  and at the top right corner at  $t = 0.65 T_{RF}$  corresponding to the sheath expansion phase at the powered electrode and at the grounded electrode, respectively. At the electrode edges and at these times, there is a superposition of a vertically and a horizontally expanding RF sheath. The latter is caused by the presence of the sidewall, which is at the same potential as the adjacent planar part of the electrode. Due to this superposition, electrons are accelerated strongly towards the reactor center by the enhanced sheath electric field at the corners. In contrast to energetic electron beams generated around  $r = 0$ , which propagate in the axial direction, these beams propagate under a certain angle with respect to the reactor axis, in accordance with experimental observations [90].

The details of the electron dynamics at the electrode edge strongly depend on the reactor design at this position. In many

commercial reactors, the sidewall is not located at the electrode edge, but at a radial distance of several cm from it. In these cases, there is typically still an edge structure and qualitatively similar effects happen, i.e. an energetic electron beam will be generated at the edge, but this beam will propagate towards the outer reactor wall. In other commercial reactors, however, the plasma is confined radially by e.g. confinement rings, whose geometry can be approximated by our simulations.

In order to compare the electron dynamics at the central region of the reactor ( $r \leq 6$  cm) to the dynamics near the sidewall, the axially and temporally resolved total ionization rate as well as its components caused by the different groups of electrons in the central region and in the edge region of the reactor are shown in figure 5. In our simulations, we also include ionization caused by  $Ar^+$  ions that occurs mostly in the vicinity of the electrodes, where the ions have been accelerated

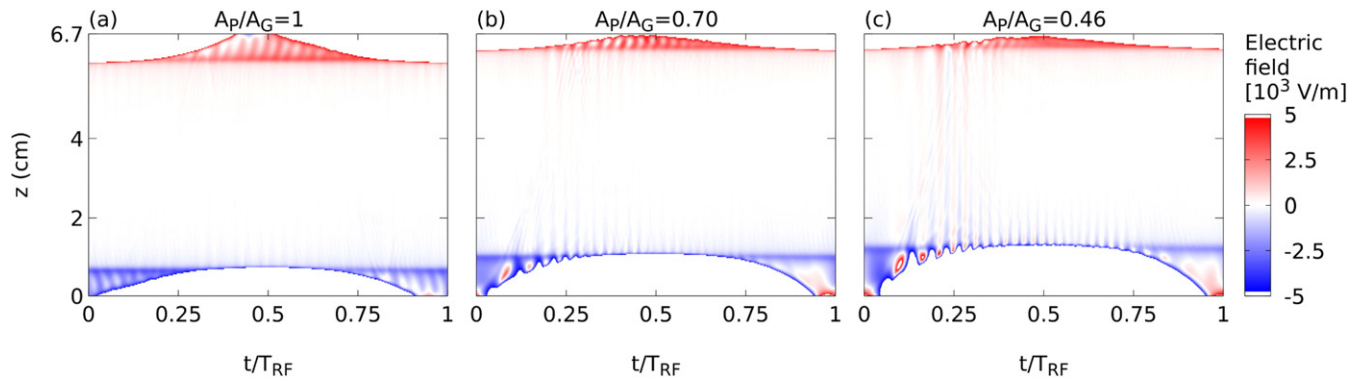


**Figure 6.** Axially and temporally resolved electric field for different reactor geometries. The results are obtained by averaging the data in the radial direction within the center region of the reactor ( $r \leq 6$  cm). The discharge conditions are the same as in figure 3.

to sufficiently high energies by the sheath electric field. As the ionization caused by ions is much weaker compared to the ionization caused by electrons, we only show the ionization rates induced by electrons here. These data are obtained by averaging the ionization rate in the radial direction within the regions of interest corresponding to  $r \leq 6$  cm and  $6 \text{ cm} < r \leq 12$  cm. Although ionization peaks are generated at the corners, as shown in figures 4(b) and (f), the ionization dynamics in the axial direction are similar in the central and the edge region, but the absolute values of the ionization rates are lower at the edge due to the lower local plasma density. This is also true for the geometrically asymmetric discharges. Therefore, we will only discuss the axially and temporally resolved electron dynamics in the central region in the following.

The radially averaged, axially and temporally resolved electric field distributions for the different reactor geometries are shown in figure 6. As a consequence of the generation of a negative DC self-bias and the depleted electron density, the sheath at the powered electrode becomes larger in the asymmetric discharges, as shown in figures 6(b) and (c). This results in a fast sheath movement at the powered electrode and leads to strong effects on the electron power absorption dynamics. During the sheath expansion phase at the powered electrode, the fast movement of the sheath leads to strong high frequency oscillations of the sheath width, which enhance the electron power absorption and cause the generation of several energetic electron beams (see the 2nd and 3rd columns of figure 7) [14, 91]. This phenomenon has been analyzed before and is related to the self-excitation of the PSR, which is more pronounced in asymmetric reactors compared to symmetric scenarios [15, 17, 69]. During the sheath collapse phase at the powered electrode, this fast movement of the sheath edge is one important reason for the generation of a strong electric field reversal, as it is hard for the electrons to follow the sheath collapse in these cases by diffusion due to their inertia [92, 93]. Other reasons for the generation of the field reversal in the asymmetric discharge are the enhanced  $\gamma$ -electron emission at the powered electrode [94, 95] and the reduced sheath collapse time. Due to the large sheath at the powered electrode, an increased number of ions bombards the electrode with high energies. Due to the energy dependence of the ion induced SEE, this leads to a

stronger emission of  $\gamma$ -electrons at this electrode. These emitted  $\gamma$ -electrons effectively lead to a decreased electron flux to the powered electrode. Moreover, the electrons can only hit the electrode during the sheath collapse, when the sheath potential is low enough for the electrons to overcome it. As the large sheath at the powered electrode collapses only for a short period of time, a large reversed electric field is generated during the sheath collapse to accelerate electrons towards the powered electrode to compensate the ion flux on time average.

The axially and temporally resolved total ionization rate as well as the ionization rate of different electron groups for the various reactor geometries are shown in figure 7. With the increase of the geometric reactor asymmetry, the ionization rate during the sheath expansion at the grounded electrode is reduced. This is the main reason for the depleted plasma density in the asymmetric discharges. This phenomenon is caused by the reduced sheath width and the reduced electron power absorption by the expanding sheath at this side of the chamber. At the powered electrode, increasing the asymmetry leads to the generation of several ionization peaks during a single sheath expansion phase, as shown in figures 7(b1) and (c1) due to the self-excitation of the PSR in these asymmetric discharges.

During the sheath collapse at the grounded electrode, strong ionization in both the symmetric and asymmetric settings is observed, as shown in figures 7(a1)–(c1). These ionization maxima are caused by energetic electron beams generated at the grounded electrode during the local sheath collapse. Figures 7(a2)–(a4) show that these electron beams mainly consist of energetic  $\delta$ -electrons in the symmetric scenario. In the asymmetric discharges, however, bulk electrons also contribute to this ionization maximum. While only a single energetic electron beam is generated by sheath expansion heating at each electrode in the symmetric scenario, multiple beams are observed in the asymmetric reactors due to the self excitation of the PSR. This modifies the time, when beam electrons impinge at the opposite electrode. While beam electrons reach the opposite electrode during the complete sheath collapse in the symmetric scenario, some beam electrons impinge earlier in the asymmetric reactor and are reflected by the residual sheath. These bulk electrons can also contribute to the ionization, as shown in figures 7(b2) and (c2). In figure 7(b4),

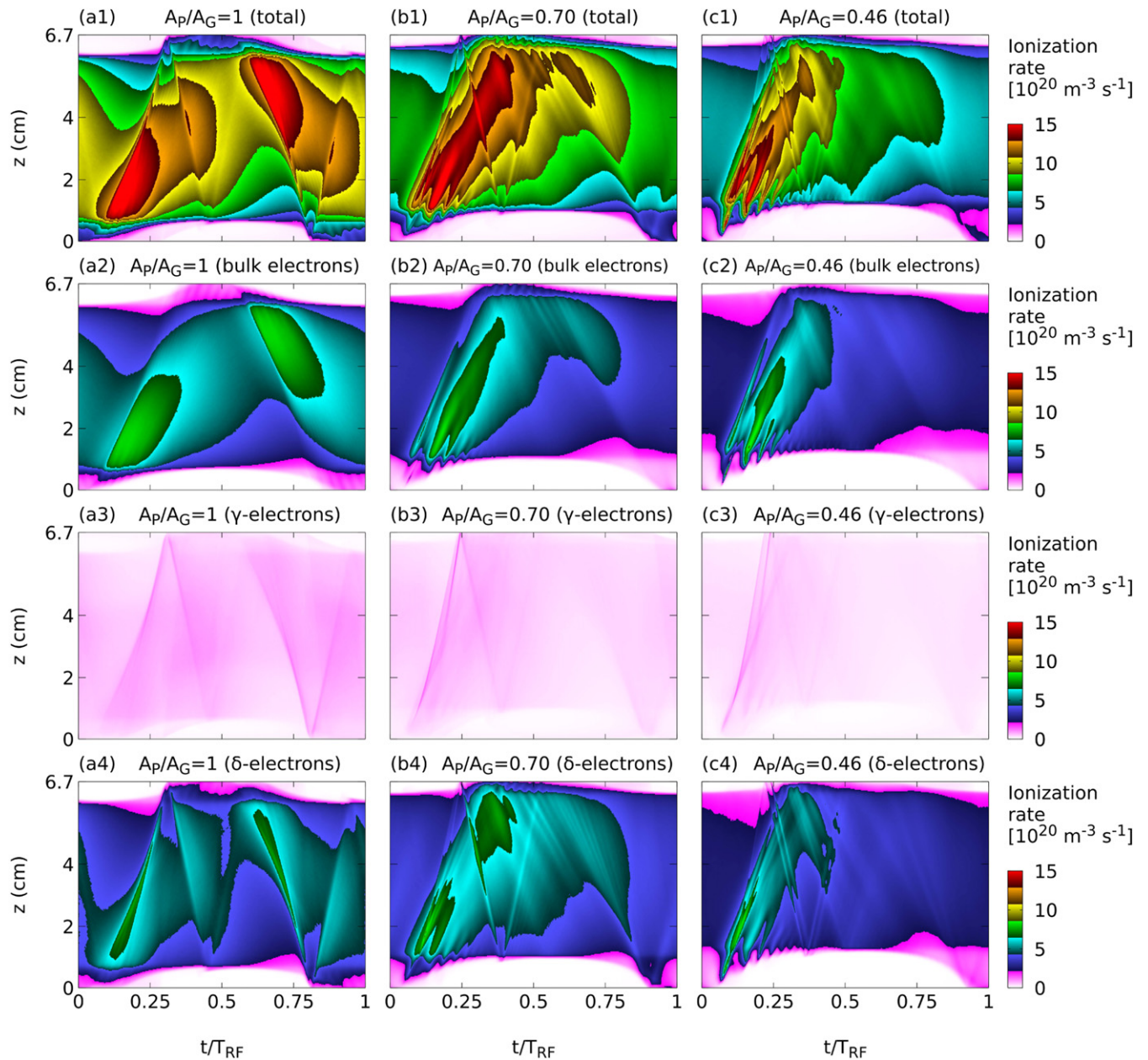


**Figure 7.** Axially and temporally resolved plots of the total ionization rate (first row), the ionization rate of bulk electrons (second row),  $\gamma$ -electrons (third row), and  $\delta$ -electrons (fourth row) for different reactor geometries. These results are obtained by averaging the data in the radial direction within the center region of the chamber ( $r < 6$  cm). The discharge conditions are the same as in figure 3.

the ionization induced by  $\delta$ -electrons is found to greatly contribute to this ionization peak during the sheath collapse at the grounded electrode in the case of  $A_P/A_G = 0.7$ . This ionization rate is higher than those in figures 7(a4) and (c4). Compared to the symmetric discharge, the stronger ionization in figure 7(b4) is mainly caused by two mechanisms: firstly, electrons are accelerated to higher energies by the fast sheath expansion at the powered electrode. Secondly, the sheath at the grounded electrode collapses for a longer fraction of the RF period due to the reactor asymmetry. Thus, incident electrons can bombard the grounded electrode with higher energies for a longer time and can cause the emission of a larger number of  $\delta$ -electrons. In the case  $A_P/A_G = 0.46$ , these two mechanisms

also exist and become even more significant, but the electron density is too low so that a lower number of electrons is emitted at the grounded electrode compared to the other geometries. Therefore, the ionization rate during the sheath collapse at the grounded electrode in figure 7(c4) is lower.

Due to the large driving voltage amplitude the sheath voltages are high and positive ions bombard the electrodes with high energies. As a consequence of the energy dependent ion induced SEECs, this leads to a large number of emitted  $\gamma$ -electrons at the electrodes. The effective  $\gamma$ -coefficients at the planar parts of the powered (bottom)/grounded (top) electrodes are 0.15/0.15; 0.26/0.07; and 0.29/0.06, respectively, for the different  $A_P/A_G$  ratios. The  $\gamma$ -electrons are acceler-

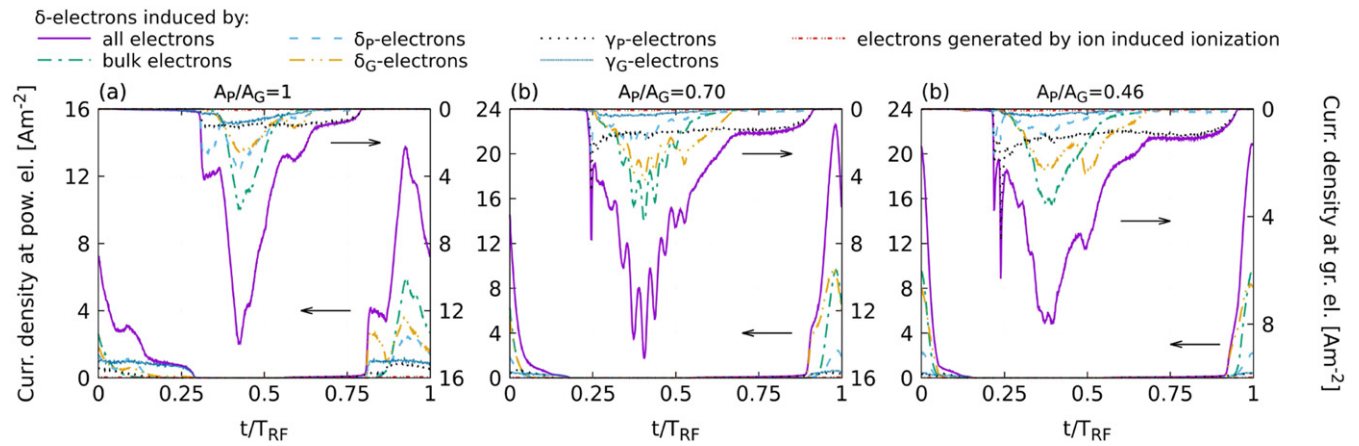


**Figure 8.** Time dependent current density of emitted  $\delta$ -electrons induced by different electron groups at the grounded (top and right axes) and powered (bottom and left axes) electrodes. The discharge conditions are the same as in figure 3.

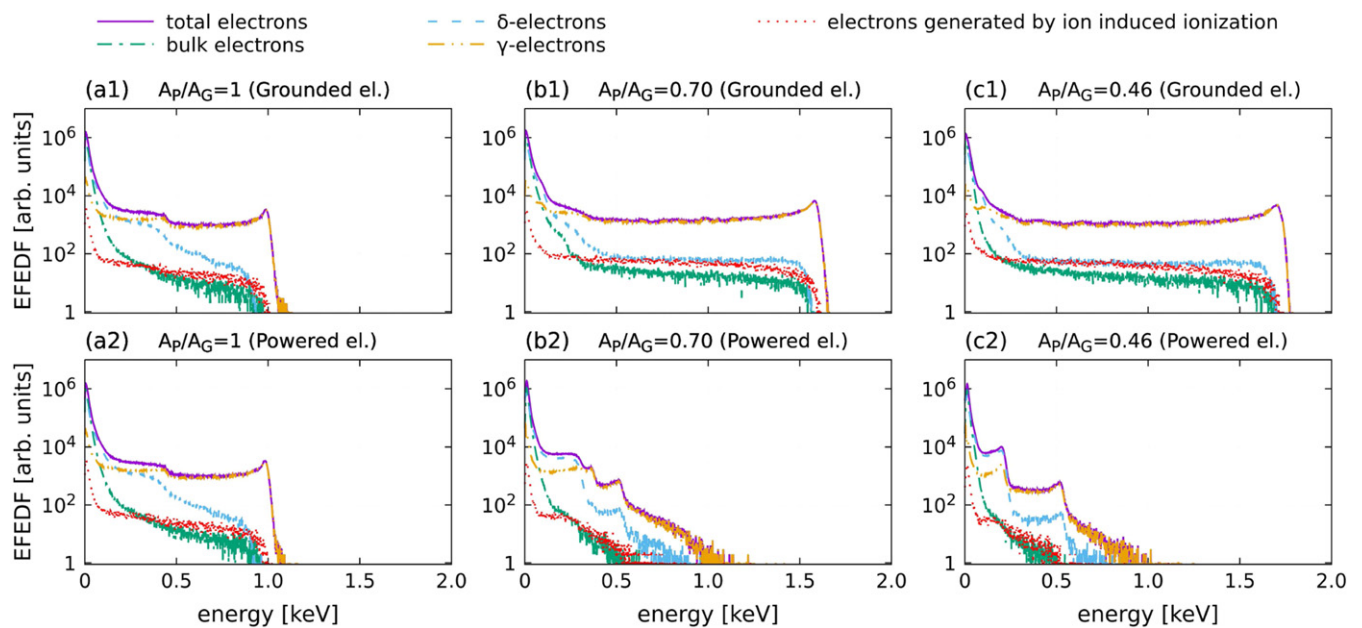


**Figure 9.** Electron flux-energy distribution function (EFEDF) at the grounded electrode (first row) and at the powered electrode (second row) for different reactor geometries. The data are spatially averaged in radial direction across the planar parts of the respective electrode. The discharge conditions are the same as in figure 3.

ated towards the plasma bulk by the sheath electric field. Nevertheless, the direct contribution of  $\gamma$ -electrons to the total ionization is low, i.e. 6.4%, 5.1%, 4.6% for  $A_P/A_G = 1$ ,  $A_P/A_G = 0.70$  and  $A_P/A_G = 0.46$ , respectively. This is because these  $\gamma$ -electrons are accelerated collisionlessly to energies in the sheath, which are too high to cause ionization efficiently. Especially in the asymmetric discharges and at the powered electrode, the  $\gamma$ -electron energy can reach up to 1.7 keV. However, these  $\gamma$ -electrons still play an important role, because they are one of the main sources of  $\delta$ -electron emission, especially in asymmetric discharges, after propagating collisionlessly through the plasma and impinging at the opposite electrode at high energies. The  $\delta$ -electrons strongly contribute to the total ionization: around 44%, 51% and 47% of the total ionization is caused directly by  $\delta$ -electrons in the

three discharge geometries, respectively. These results show that both the  $\gamma$ - and  $\delta$ -electrons play very important (geometry dependent) roles in geometrically symmetric and asymmetric discharges operated at low pressure and high voltage.

The time dependent current densities of emitted  $\delta$ -electrons induced by different electron groups at the grounded and at the powered electrode are shown in figure 8. In the symmetric discharge, three peaks of the total  $\delta$ -electron emission are observed at the grounded electrode. As shown in figure 8(a), most of the  $\delta$ -electrons are emitted at the time around  $t/T_{RF} = 0.45$  at the grounded electrode when the local sheath collapses. These  $\delta$ -electrons are mostly emitted by bulk electrons. Another  $\delta$ -electron emission peak appears at the time around  $t/T_{RF} = 0.35$ , which is mainly caused by the  $\delta$ -electrons originating from the powered electrode. They are

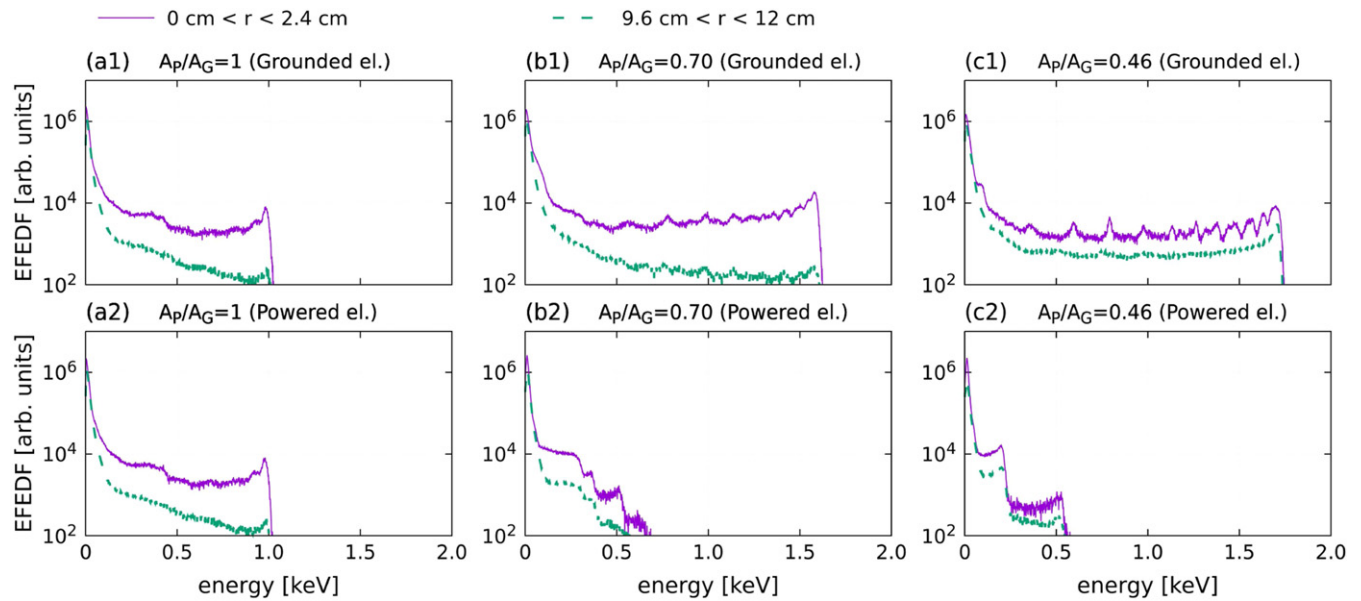


**Figure 10.** Total electron-flux energy distribution function within the region  $0 \text{ cm} < r < 2.4 \text{ cm}$  and  $9.6 \text{ cm} < r < 12 \text{ cm}$  of the top (grounded) electrode (first row) and the (bottom) powered electrode (second row). The discharge conditions are the same as in figure 3.

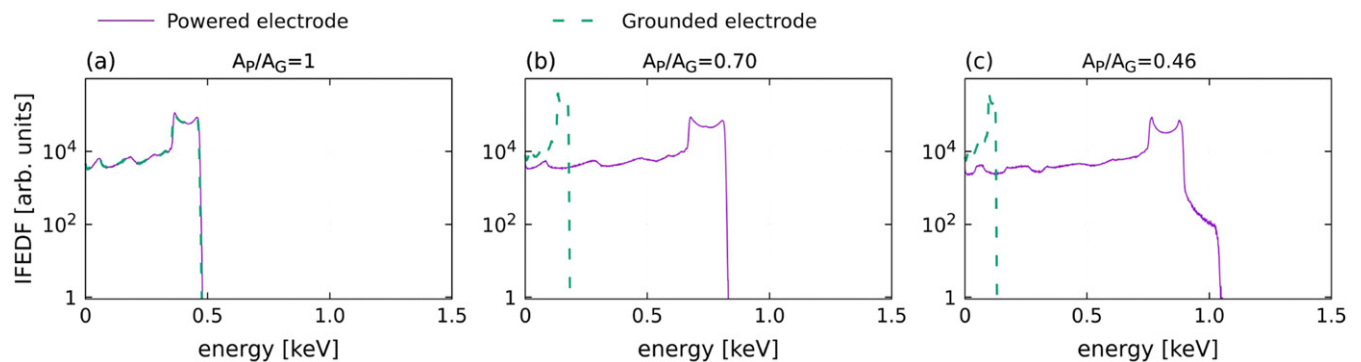


**Figure 11.** Radially averaged ion flux-energy distribution function (IFEDF) at the grounded electrode and the powered electrode at different reactor geometries. The discharge conditions are the same as in figure 3.

emitted and accelerated near the powered electrode by two different mechanisms. Firstly, most of these  $\delta$ -electrons are emitted during the local sheath collapse and stay close to the powered electrode. As soon as the sheath starts to expand, they are accelerated and move towards the grounded electrode. Compared to these  $\delta$ -electrons, most of the bulk electrons are located further away from the electrode, when they are accelerated by the expanding sheath. Therefore, the bulk electrons arrive and induce  $\delta$ -electron emission at the grounded electrode later than the  $\delta$ -electrons, which are accelerated by the expanding sheath at the powered electrode first. Secondly, another group of  $\delta$ -electrons is emitted from the powered electrode during the time when the local sheath has already started to expand. These  $\delta$ -electrons can be accelerated to high energies inside the sheath. As shown in figure 8(a), during the time  $t/T_{RF} = 0.15-0.3$ , most of the  $\delta$ -electron emissions at the powered electrode are induced by  $\gamma$ -electrons emitted at the grounded electrode. The  $\gamma$ -electrons emitted at the grounded electrode are accelerated in the local sheath to high energies,

which allows them to overcome the sheath potential at the powered electrode and to induce  $\delta$ -electron emission. In figure 8(a), the third  $\delta$ -electron emission peak at the grounded electrode appears at the time around  $t/T_{RF} = 0.55$ . The  $\delta$ -electrons generated at the grounded electrode contribute to the  $\delta$ -electron emission at this time within the RF period. As shown in figure 7(a4),  $\delta$ -electrons emitted at the grounded electrode during the local sheath collapse are reflected by the sheath at the powered electrode and propagate back towards the grounded electrode and finally bombard the grounded electrode. In this way they induce  $\delta$ -electron emission at the grounded electrode. In addition to this,  $\gamma$ -electrons generated at the powered electrode are found to induce  $\delta$ -electron emission at the grounded electrode during a long fraction of the RF period, because these  $\gamma$ -electrons can obtain high energy in the sheath at the powered electrode after they are emitted. After propagating collisionlessly through the plasma this allows them to overcome the sheath potential and hit the grounded electrode. The mechanisms of  $\delta$ -electron emission at the powered electrode in the

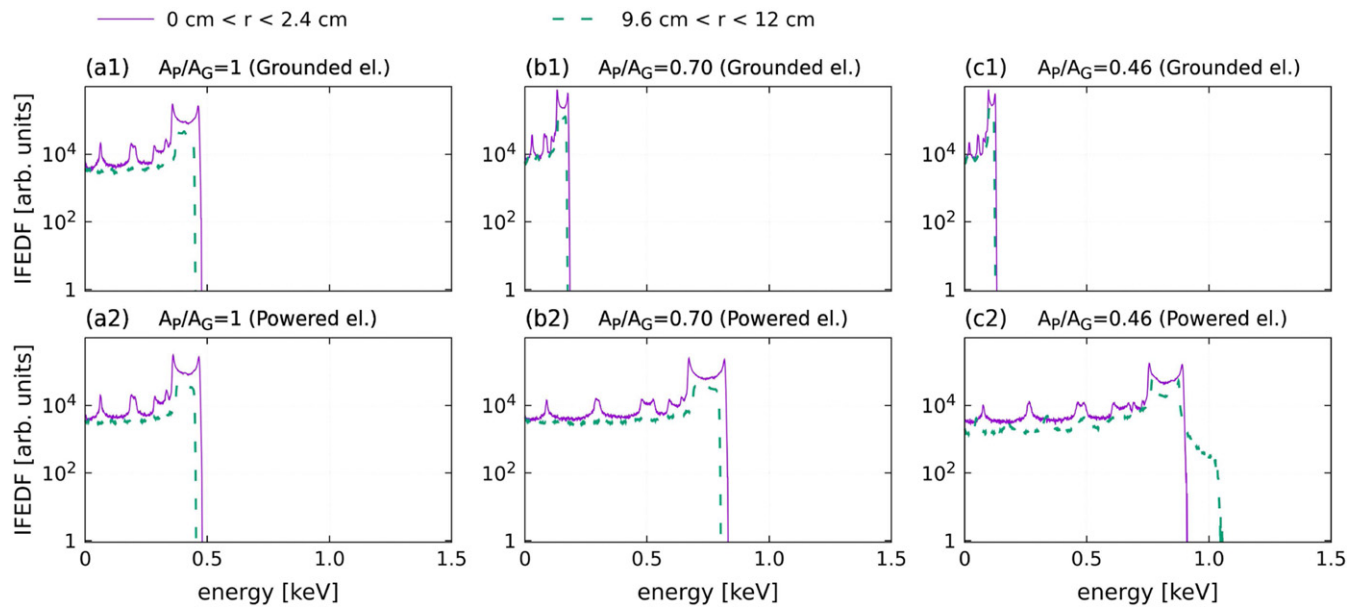


**Figure 12.** IFEDF within the regions  $0 \text{ cm} < r < 2.4 \text{ cm}$  and  $9.6 \text{ cm} < r < 12 \text{ cm}$  of the grounded (first row) and the powered (second row) electrode for different chamber geometries. The discharge conditions are the same as in figure 3.

symmetric discharge are the same as those at the grounded electrode.

In the asymmetric discharges, due to the small sheath at the grounded electrode, electrons can reach this electrode and induce  $\delta$ -electron emission during a longer fraction of the RF period compared to the situation in the symmetric scenario. As shown in figures 8(b) and (c),  $\gamma$ -electrons become the main source of  $\delta$ -electron emission at the grounded electrode in these cases. This is caused by the strong acceleration of  $\gamma$ -electrons in the large sheath at the smaller powered electrode. Due to their high bombardment energy at the grounded electrode, each of these  $\gamma$ -electrons can induce multiple  $\delta$ -electron emissions. Similar to the symmetric discharge, three large peaks of the  $\delta$ -electron emission are observed at the grounded electrode in figures 8(b) and (c). Due to the high sheath voltage at the powered electrode in the asymmetric discharges, the  $\gamma$ -electrons emitted at the grounded electrode cannot overcome the sheath potential and emit  $\delta$ -electrons at the powered electrode for most of the RF period. In this scenario, the first peak of the  $\delta$ -electron emission at the grounded electrode is mainly caused by  $\delta$ - and  $\gamma$ -electrons emitted at the powered electrode during the sheath collapse and accelerated by the local sheath expansion. Several additional small peaks of the  $\delta$ -electron emission at the grounded electrode are observed in the asymmetric discharges. These peaks are induced by the high frequency PSR sheath oscillations at the powered electrode during the local expansion phase, which lead to the generation of multiple energetic electron beams. These energetic electrons cause several  $\delta$ -electron emission peaks when they bombard the grounded electrode (note the high yields at several 100 eV energy in figure 2). At the powered electrode electrons can only induce  $\delta$ -electron emission, when the local sheath is fully collapsed since the high local sheath voltage at other times within the RF period cannot be overcome by electrons.

Therefore, much less  $\delta$ -electron emission is found at the powered electrode. As a high number of  $\delta$ -electrons is emitted at the grounded electrode, these  $\delta$ -electrons contribute strongly to the  $\delta$ -electron emission at the powered electrode in the asymmetric cases.

The total electron flux-energy distribution function (EFEDF) as well as the flux-energy distribution function of different electron groups at the (top) grounded and the (bottom) powered electrode are shown in figure 9. The data are spatially averaged in the radial direction across the planar parts of the respective electrode, electrons that bombard the sidewall are not taken into account. After being accelerated within the sheath and propagating collisionlessly through the plasma bulk, a number of  $\gamma$ -electrons bombards the opposite electrode with very high energies. In the asymmetric discharges, where a large negative DC self-bias is generated, the  $\gamma$ -electron bombardment energy at the grounded electrode can reach up to 1.7 keV. In these plots, the red dashed line indicates the distribution function of electrons generated by ion induced ionization. As positive ions are accelerated to very high energies in the sheaths, they can ionize neutrals in the vicinity of the electrodes. As a result, electrons are generated deep inside the sheath, are accelerated to high energies and bombard the opposite electrode at high energies. We also observe high energy bulk and  $\delta$ -electron bombardment of the grounded electrode in figures 9(b1) and (c1) and steps of the EFEDF in figure 9(c2). These phenomena are caused by the different dynamics of different electron groups, which will be discussed in the next section.

Figure 10 shows the total EFEDF within radial regions of  $0 \text{ cm} < r < 2.4 \text{ cm}$  and  $9.6 \text{ cm} < r < 12 \text{ cm}$  of the powered and grounded electrode. The shape of the EFEDF is found to be similar at different radii, but due to the decreased electron density towards the sidewall, fewer electrons bombard the

**Table 1.** Surface coefficients and peak electron density for the cases studied in section 3.2.

#	$\gamma$ -Coefficient (powered el./grounded el.)	$\delta$ -Coefficient (powered el./grounded el.)	Peak density
Case 1	0/0	0/0	$1.03 \times 10^{16} \text{ m}^{-3}$
Case 2	Oxid. surf./oxid. surf.	0/0	$1.13 \times 10^{16} \text{ m}^{-3}$
Case 3	0/0	SiO <sub>2</sub> /SiO <sub>2</sub>	$1.19 \times 10^{16} \text{ m}^{-3}$
Case 4	Oxid. surf./oxid. surf.	SiO <sub>2</sub> /SiO <sub>2</sub>	$1.53 \times 10^{16} \text{ m}^{-3}$
Case 5	Oxid. surf./0	SiO <sub>2</sub> /0	$1.13 \times 10^{16} \text{ m}^{-3}$
Case 6	0/Oxid. surf.	0/SiO <sub>2</sub>	$1.20 \times 10^{16} \text{ m}^{-3}$

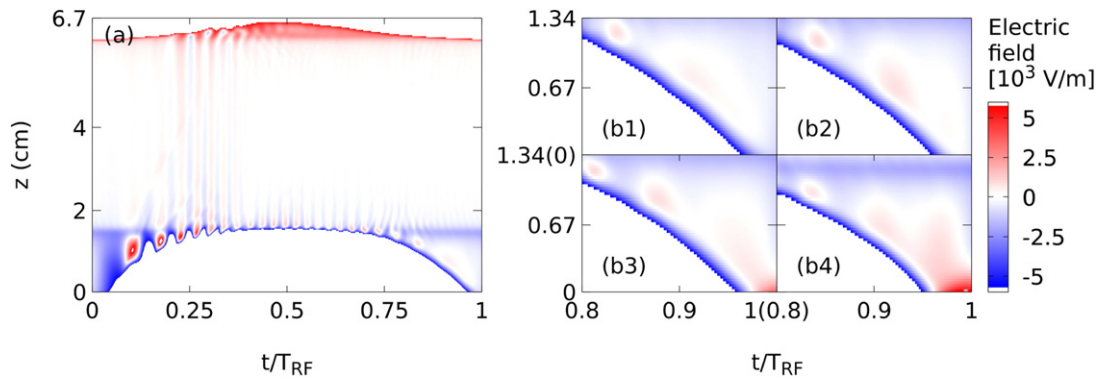


**Figure 13.** Axially and temporally resolved electric field for different surface SEEC conditions:  $\gamma = 0, \delta = 0$  (case 1) in (a) and (b1);  $\gamma = \gamma_{\text{oxid.}}, \delta = 0$  (case 2) in (b2);  $\gamma = 0, \delta = \delta_{\text{SiO}_2}$  (case 3) in (b3); and  $\gamma = \gamma_{\text{oxid.}}, \delta = \delta_{\text{SiO}_2}$  (case 4) in (b4). The results are obtained by averaging the data in the radial direction within the center region of the chamber ( $r < 6$  cm). The discharge conditions are the same as in figure 3.

electrode in the region  $9.6 \text{ cm} < r < 12 \text{ cm}$ . Moreover, compared to the case  $A_P/A_G = 0.46$ , a larger difference between the number of high energy electrons bombarding the electrode close to its edge ( $9.6 \text{ cm} < r < 12 \text{ cm}$ ) and center ( $0 \text{ cm} < r < 2.4 \text{ cm}$ ) is found in the cases of  $A_P/A_G = 1$  and  $0.7$ . This is mostly caused by the different effect of the sidewall sheath on the propagation of highly energetic  $\gamma$ -electrons from one electrode to the other close to the electrode edge in case of different geometric reactor asymmetries. For instance,  $\gamma$ -electrons emitted at the planar part of the bottom electrode close to the sidewall are accelerated horizontally by the adjacent sheath next to the powered fraction of the sidewall on their way towards the opposite electrode and move towards the discharge center. This effect is more pronounced in the symmetric compared to the asymmetric scenario, since a larger fraction of the sidewall is powered in the symmetric case. In the asymmetric cases, the sidewall sheath adjacent to the grounded wall is small and oscillates  $180^\circ$  out of phase compared to the sheath at the powered electrode, i.e. it is collapsed, when  $\gamma$ -electrons are accelerated to high energies at the powered electrode. Therefore, less energetic electrons bombard the opposite electrode close to its edge in the more symmetric scenarios.

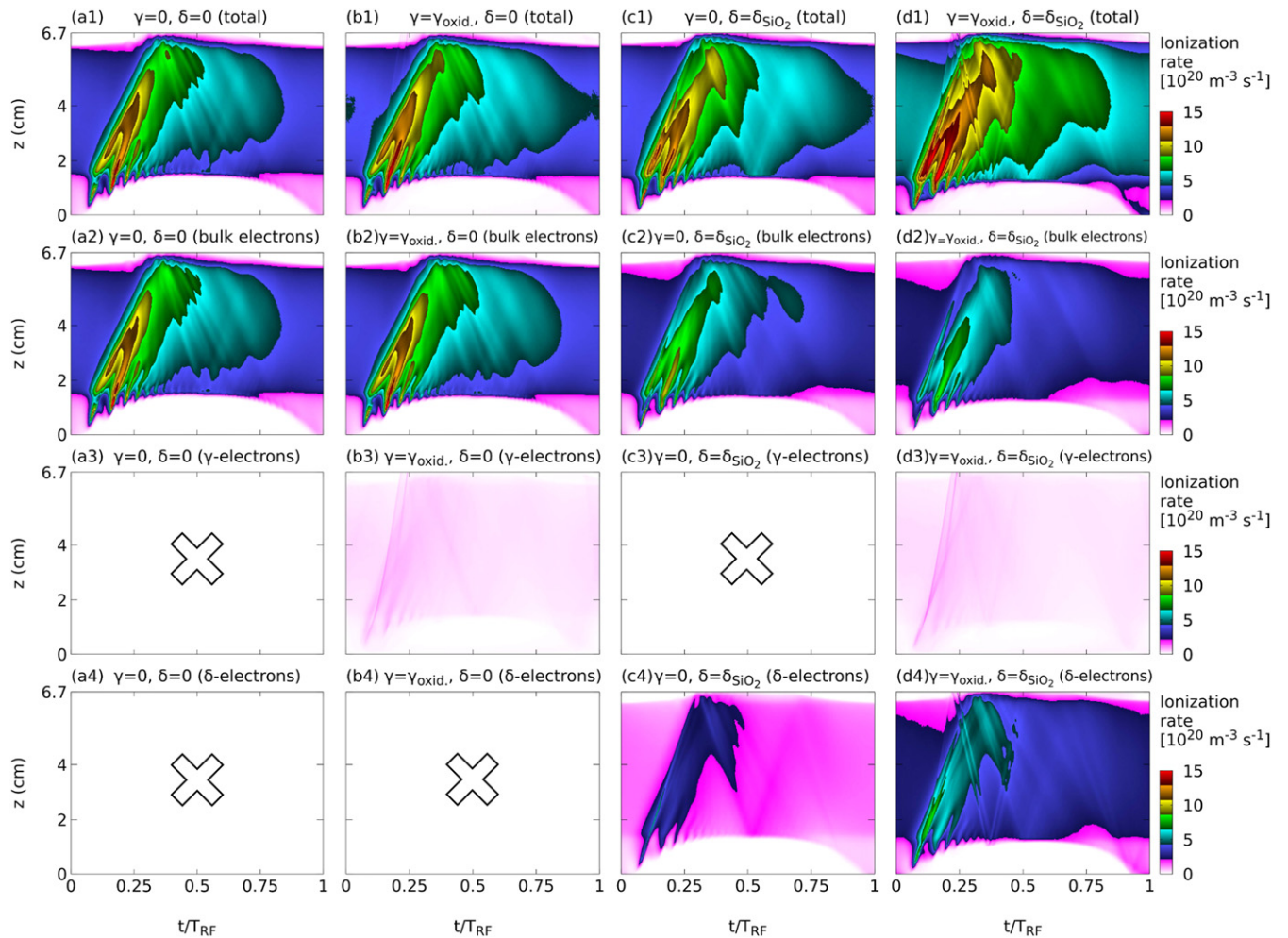
The radially averaged IFEDFs at the planar part of the grounded and the powered electrodes are shown in figure 11. It is found that by decreasing the area ratio of the powered and grounded electrode, the maximum ion energy increases at the powered electrode, but decreases at the grounded electrode as a consequence of the generation of a negative DC self-bias caused by the geometric reactor asymmetry.

Figure 12 shows the IFEDF within different radial regions of interest at the planar part of the powered and grounded electrodes. Several peaks are observed at low energies in addition to the bimodal shape at high energies. These peaks are caused by charge exchange collisions of ions inside the sheaths [96]. In figure 12(c2), higher energy ion bombardment at the powered electrode is found in the region  $9.6 \text{ cm} < r < 12 \text{ cm}$  compared to other regions. This is because in the case  $A_P/A_G = 0.46$ , the powered electrode and the grounded electrode are connected via the dielectric spacer at the bottom electrode edge, which leads to an enhanced electric field at this position. Therefore, the ions near the electrode edge can be accelerated by the enhanced electric field and bombard the bottom electrode at higher energies.

### 3.2. The effects of individual surface coefficients on the charged particle dynamics

The results presented in the previous section showed that secondary electrons play an important role for the charged particle dynamics. To further understand the effects of different secondary electron groups on the discharge and electron energy distribution functions at boundary surfaces, the ion and electron induced SEECs of the electrodes are varied systematically in this section. We study the effects of four different choices of the surface coefficients in the most asymmetric scenario of  $A_P/A_G = 0.46$ , i.e. the first four cases listed in table 1.

The last column of table 1 lists the peak electron density for these cases. Including only  $\gamma$ -electrons (case 2) or only  $\delta$ -electrons (case 3) leads to a similar increase of the plasma



**Figure 14.** Axial and temporal distribution of the total ionization rate (first row), the ionization rate of bulk electrons (second row),  $\gamma$ -electrons (third row), and  $\delta$ -electrons (fourth row) for different surface SEEC conditions. The results are obtained by averaging the data in the radial direction within the center region of the chamber ( $r < 6$  cm). The discharge conditions are the same as in figure 3.

density compared to the scenario where SEE is neglected completely (case 1). If both,  $\gamma$ - and  $\delta$ -electrons, are included (case 4), the plasma density increases much stronger, i.e. by more than the sum of the individual effects of including only one type of SEE. The reason for this synergy is the coupling between both processes as discussed before, i.e. energetic  $\gamma$ -electrons are a major source of  $\delta$ -electron emission. Clearly, both SEE processes must be included for correct simulation results at the given operating conditions. Changing the surface coefficients in this way slightly affects the DC self-bias ( $-661$  V for  $\gamma = \delta = 0$ ,  $-653$  V for  $\gamma = \gamma_{\text{oxid.}}$ ,  $\delta = 0$ ,  $-694$  V for  $\gamma = 0$ ,  $\delta = \delta_{\text{SiO}_2}$ , and  $-712$  V for  $\gamma = \gamma_{\text{oxid.}}$ ,  $\delta = \delta_{\text{SiO}_2}$ ).

Figure 13 shows the axially and temporally resolved electric field for these four cases. These results are obtained by averaging the data in the radial direction within the center region of the chamber ( $r < 6$  cm). In general, a large sheath is formed at the smaller powered electrode due to the strongly negative DC self-bias. During the sheath expansion phase, strong oscillations appear due to the self-excitation of the PSR, as shown in figure 13(a). During the sheath collapse phase the different surface coefficients lead to different strengths of

the electric field reversal. Figures 13(b1)–(b4) show the electric field near the powered electrode during the sheath collapse phase for these four cases. The reversed electric field is enhanced by including either the  $\gamma$ -electrons or the  $\delta$ -electrons, and is most pronounced if both these SEECs are included in the simulation. This is caused by a decrease of the net electron flux towards the electrode in the presence of strong electron emission.

The axially and temporally resolved plots of the ionization rate for different electron groups are shown in figure 14. Again, the data are averaged radially in the central region of the reactor. The crosses in some of the plots indicate that the corresponding electron species is not considered in the given case. The total ionization rate is strongest for the case, where both the  $\gamma$ - and  $\delta$ -electrons are included (case 4), especially during the sheath collapse phase at the grounded electrode, when  $\delta$ -electrons contribute strongly to the ionization. In the third case ( $\gamma = 0$ ,  $\delta = \delta_{\text{SiO}_2}$ ), the  $\delta$ -electron emission is much weaker than for the case that includes both SEE mechanisms. As discussed in the first section, the  $\gamma$ -electrons play a major role for  $\delta$ -electron emission at the grounded electrode in the asymmetric discharges. In the third case ( $\gamma = 0$ ,  $\delta = \delta_{\text{SiO}_2}$ ), the

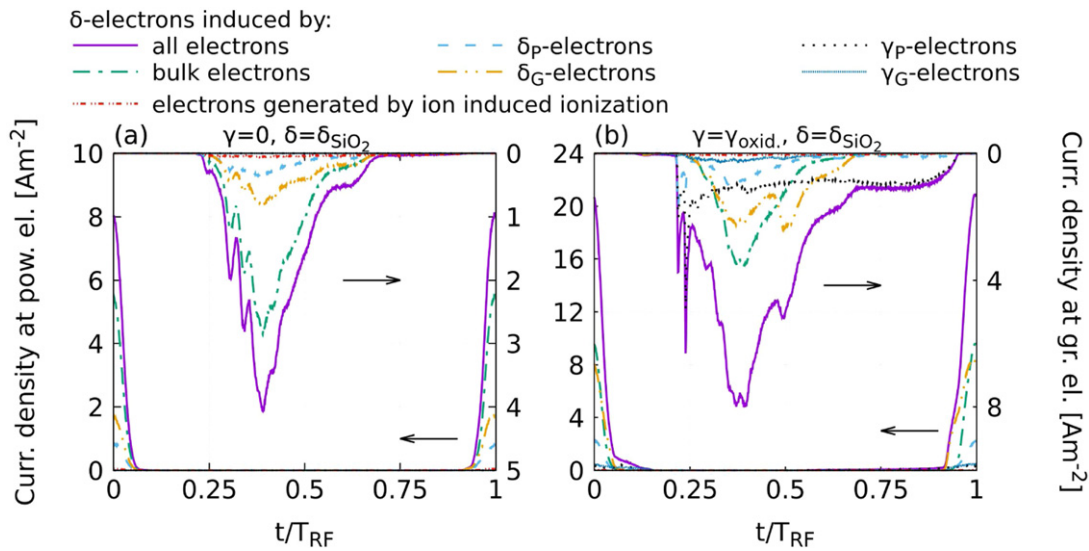


**Figure 15.** Time resolved current density of emitted  $\delta$ -electrons induced by different electron groups at the grounded electrode (top and right axes) and the powered electrode (bottom and left axes) with  $\gamma = 0$ ,  $\delta = \delta_{\text{SiO}_2}$  (case 3) in (a), and  $\gamma = \gamma_{\text{oxid.}}$ ,  $\delta = \delta_{\text{SiO}_2}$  (case 4) in (b). The discharge conditions are the same as in figure 3.

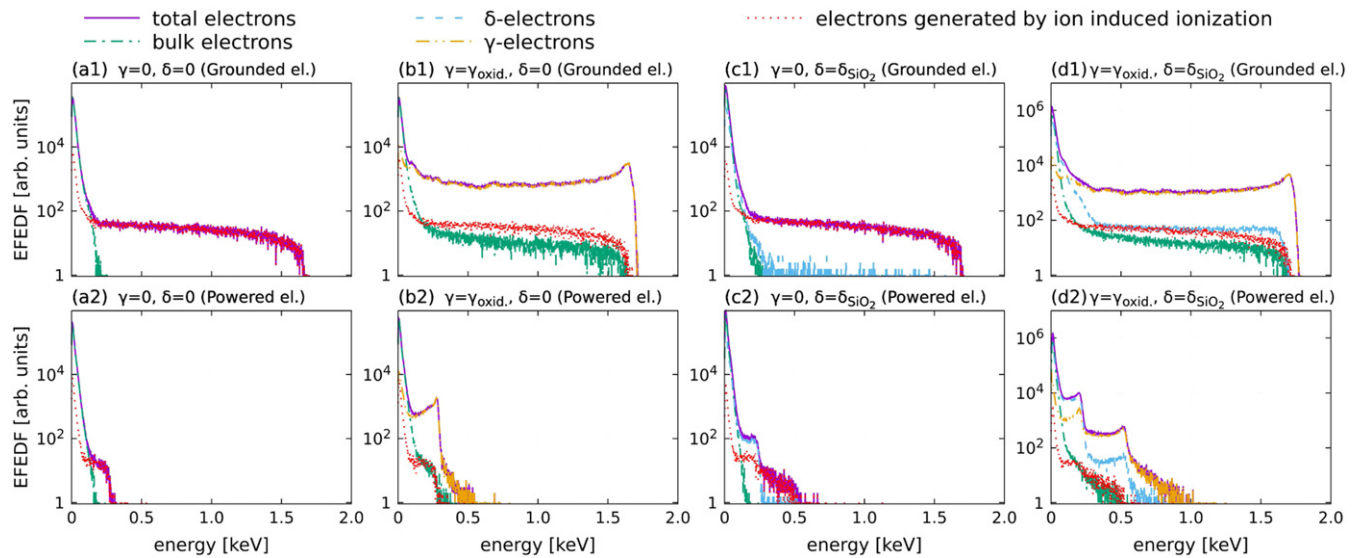


**Figure 16.** Electron flux-energy distribution function at the grounded (first row) and at the powered electrode (second row) for different surface SEEC conditions. The data are radially averaged across the planar part of the respective electrode. The discharge conditions are the same as in figure 3.

bulk electrons become the most important source of  $\delta$ -electron emission. As the bulk electron bombardment energies at the electrodes are lower than those of  $\gamma$ -electrons, much fewer  $\delta$ -electrons are emitted at the grounded electrode, as shown in figure 15. Figures 14(c4) and (d4) show the ionization rate caused by the  $\delta$ -electrons in the last two cases ( $\gamma = 0$ ,  $\delta = \delta_{\text{SiO}_2}$  and  $\gamma = \gamma_{\text{oxid.}}$ ,  $\delta = \delta_{\text{SiO}_2}$ ). For  $\gamma = 0$ ,  $\delta = \delta_{\text{SiO}_2}$ , the  $\delta$ -electrons cause 30% of the total ionization, which is much less than in the case of  $\gamma = \gamma_{\text{oxid.}}$ ,  $\delta = \delta_{\text{SiO}_2}$ , where the  $\delta$ -electrons cause 47% of the total ionization directly. As a result of this, the plasma density is higher in the last case.

Figure 15 shows the time resolved current density of emitted  $\delta$ -electrons in the case of  $\gamma = 0$ ,  $\delta = \delta_{\text{SiO}_2}$  (a) and  $\gamma = \gamma_{\text{oxid.}}$ ,

$\delta = \delta_{\text{SiO}_2}$  (b), respectively. In the case of  $\gamma = 0$ , much fewer  $\delta$ -electrons are emitted at both the powered and the grounded electrode, due to the absence of  $\gamma$ -electrons. Most of the  $\delta$ -electron emissions at the grounded electrode are induced by bulk electrons in this case. For  $\gamma = \gamma_{\text{oxid.}}$ , the  $\gamma$ -electrons from the powered electrode make the largest contribution to the  $\delta$ -electron emission at the grounded electrode. Due to the high energies of these  $\gamma$ -electrons and the small sheath at the grounded electrode, the  $\delta$ -electrons can be emitted during a long fraction of the RF period. In figure 15(b), a  $\delta$ -electron emission peak at the grounded electrode can be observed at  $t/T_{\text{RF}} = 0.5$ . This peak is caused by the  $\delta$ -electrons generated at the grounded electrode. Figure 14(d4) shows that two

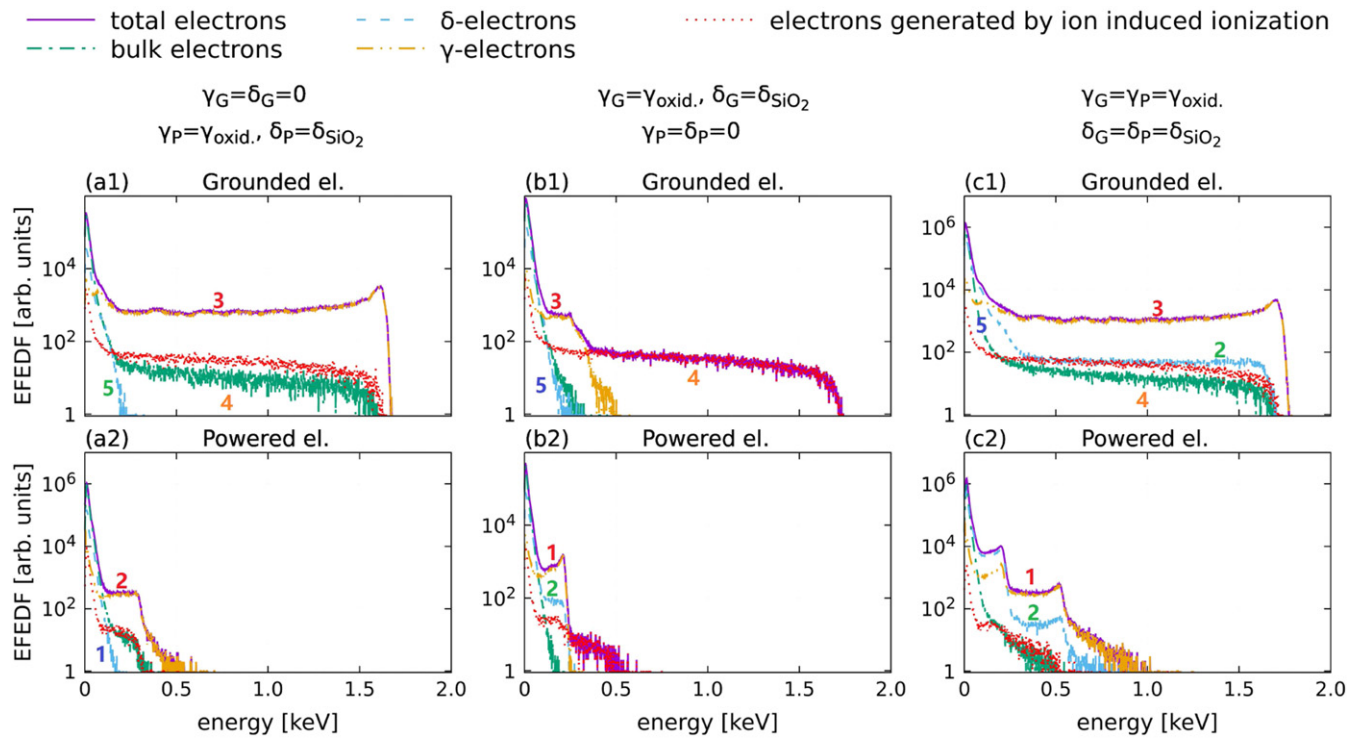


**Figure 17.** Electron flux–energy distribution function at the grounded electrode (first row) and the powered electrode (second row) for different surface SEEC conditions. The data are radially averaged across the planar part of the respective electrode. Here,  $\gamma_G$  and  $\delta_G$  represent the  $\gamma$  and  $\delta$  coefficients at the grounded electrode,  $\gamma_P$  and  $\delta_P$  represent the  $\gamma$  and  $\delta$  coefficients at the powered electrode. The discharge conditions are the same as in figure 13.

beams of  $\delta$ -electrons are formed at the grounded electrode at  $t/T_{RF} \approx 0.25$ . Based on figure 15(b), these  $\delta$ -electrons are mostly emitted due to  $\gamma$ -electron impact at the grounded electrode. After being emitted, these  $\delta$ -electrons are reflected by the large sheath at the powered electrode and finally bombard the grounded electrode and lead to the  $\delta$ -electron emission peak at  $t/T_{RF} = 0.5$ . As there is no  $\gamma$ -electron induced  $\delta$ -electron emission at  $t/T_{RF} = 0.25$  in the case of  $\gamma = 0$ , the peak at  $t/T_{RF} = 0.5$  is absent in figure 15(a). Moreover, due to the high number of emitted  $\delta$ -electrons at the grounded electrode in the case of  $\gamma = \gamma_{oxid}$ , a large number of  $\delta$ -electron emissions at the powered electrode is caused by these  $\delta$ -electrons. For  $\gamma = 0$ , most of the  $\delta$ -electron emissions at the powered electrode are induced by bulk electrons.

The EFEDFs of different electron groups at the electrodes are shown in figure 16 for the first four cases specified in table 1. In the presence of  $\gamma$ -electrons (figures 16(b1) and (d1)), high energy bulk electron bombardment at the grounded electrode is observed, which disappears in the absence of  $\gamma$ -electrons (figures 16(a1) and (c1)). These electrons are generated by ionization induced by  $\gamma$ -electrons in the vicinity of the powered electrode inside the sheath. These bulk electrons can then be accelerated towards the plasma bulk in the large sheath and, therefore, bombard the grounded electrode at high energies.

The number of high energy  $\delta$ -electrons at the grounded electrode is much higher for  $\gamma = \gamma_{oxid}$ ,  $\delta = \delta_{SiO_2}$  (figure 16(d1)) compared to  $\gamma = 0$ ,  $\delta = \delta_{SiO_2}$  (figure 16(c1)). As will be discussed in more detail below, these high energy  $\delta$ -electrons

are generated by  $\gamma$ -electron impact at the powered electrode at times of high local sheath voltage, when the newly generated  $\delta$ -electrons are accelerated towards the bulk to high energies by the high instantaneous local sheath electric field.

In the presence of  $\gamma$ -electrons, figures 16(b2) and (d2) show that a relatively high number of  $\gamma$ -electrons bombards the powered electrode. Their energy distribution exhibits multiple steps at high energies. To understand their formation, further insights into the dynamics of different electron groups are required. In the following, we will, therefore, perform a detailed analysis. Firstly, we clarify the origin of electrons in each part of the EFEDFs at both electrodes. A similar analysis has been conducted recently by Fu *et al* [97] to illustrate the kinetic behaviour of high-energy ballistic electrons in low pressure discharges and by Vass *et al* [98] to explain the complex features of different physical quantities inside the sheath, which are caused by the spatio-temporal dynamics of fast electrons and their interaction with the sheath electric field.

To obtain these insights, we use different combinations of SEECs at the powered and grounded electrode and compare the radially averaged EFEDFs at the surface of the planar parts of the electrodes obtained for three different cases in figure 17, i.e. cases 4–6 listed in table 1. To better understand the complex electron dynamics in these cases, we show the corresponding time resolved electron flux–energy distribution function (EFEDF) in figure 18 and schematics of individual electron trajectories in figure 19. The first columns of these figures show results for the case 5 in table 1, which is

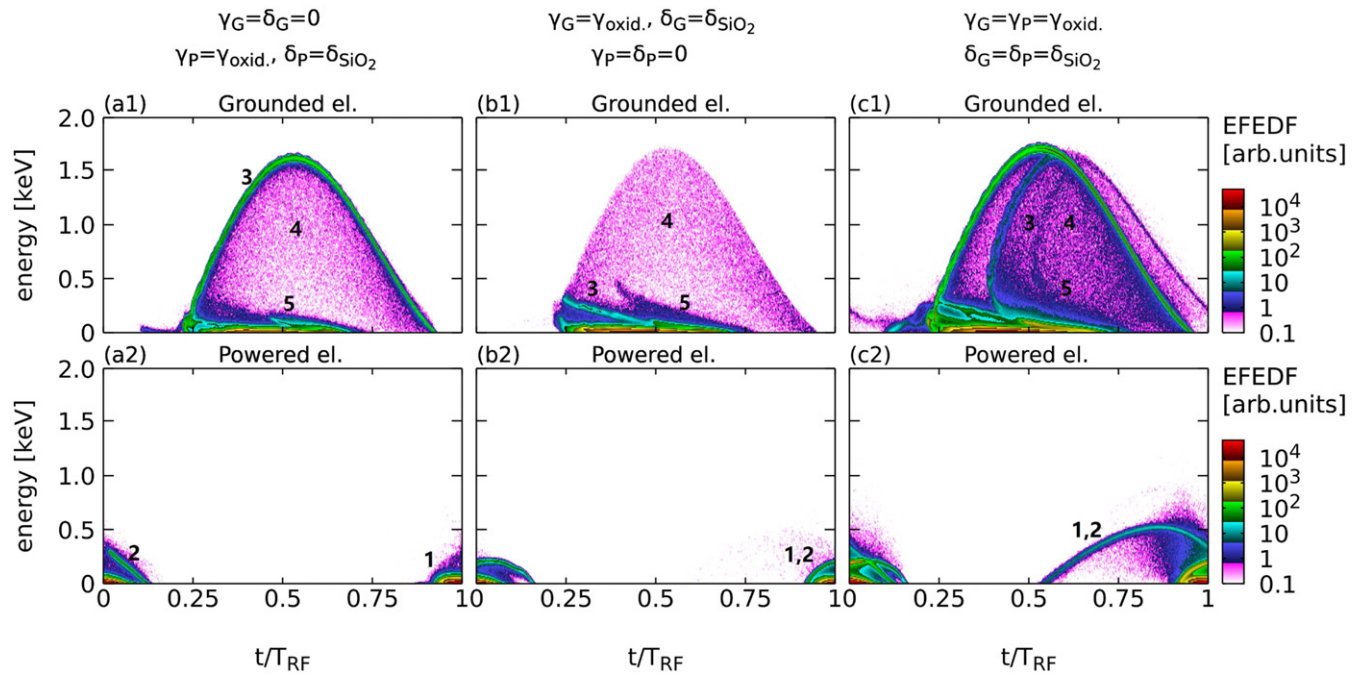


**Figure 18.** Time resolved electron flux–energy distribution function at the grounded electrode (first row) and the powered electrode (second row) at different SEEC conditions. The data are radially averaged across the planar part of the respective electrode. The discharge conditions are the same as in figure 3.

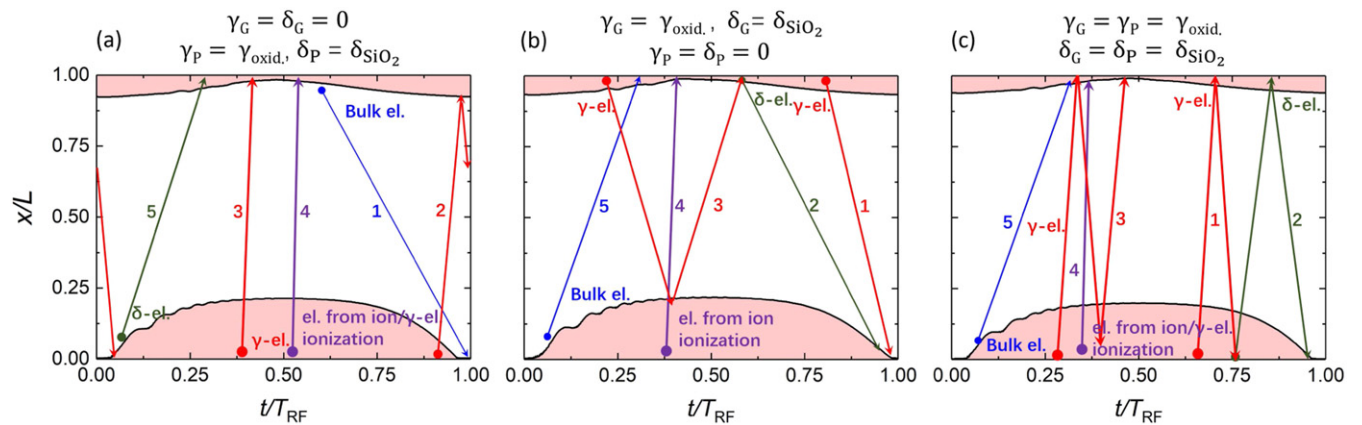


**Figure 19.** Schematic trajectories of individual electrons for different surface SEEC conditions. The light pink zones indicate the sheath regions.

obtained based on  $\gamma$  and  $\delta$ -coefficients for a  $\text{SiO}_2$  surface at the powered electrode, but  $\gamma = \delta = 0$  at the grounded electrode. A large arc marked as ‘3’ is found in figure 18(a1), which indicates electron bombardment at the grounded electrode with energies up to around 1.7 keV. As shown in figure 19(a) with the arrow ‘3’, these are the  $\gamma$ -electrons emitted at the powered electrode. After being emitted, they are accelerated in the large sheath and finally bombard the grounded electrode at high energies. As shown in figure 18(a2) and marked as ‘1’, many electrons bombard the powered electrode at the time around  $t/T_{\text{RF}} = 0$  and 1, when the local sheath is collapsed. Besides this, a green oblique line marked as ‘2’ appears at  $t/T_{\text{RF}} = 0$ , which indicates that a number of electrons bombards the powered electrode with a higher energy (up to about 400 eV). From figure 17(a2) we know that these electrons are  $\gamma$ -electrons.

In this case, the  $\gamma$ -electrons are only emitted from the powered electrode and the electron reflection probability is 0 at the grounded electrode. Therefore, these high energy  $\gamma$ -electrons, which bombard the powered electrode, were emitted at the powered electrode and then reflected by the sheath at the grounded electrode, as shown in figure 19(a) by the red arrows marked as ‘2’. It should be noticed that these  $\gamma$ -electrons must be emitted when the sheath at the powered electrode has collapsed to a small width. This allows the  $\gamma$ -electrons to have a relatively low energy and to be reflected by the sheath at the grounded electrode. Otherwise they would be absorbed by the grounded electrode. In figure 17(a1), the bulk electrons and the electrons generated by ion induced ionization are found to bombard the grounded electrode with energies as high as 1.5 keV. As shown in figure 19(a) by the arrow marked as ‘4’,

these electrons are generated deeply inside the sheath at the powered electrode and can, thus, obtain very high energies in the sheath before hitting the grounded electrode.

The second column of these figures shows the results for case 6 in table 1. An ‘arc’ with green color is found in figure 18(b2), which indicates high energy electron bombardment at the powered electrode with energies up to about 300 eV. In figure 17(b2), we find that most of these electrons are  $\gamma$ -electrons. As  $\gamma$ -electrons are only emitted at the grounded electrode for this case, these  $\gamma$ -electrons are accelerated in the sheath and then bombard the powered electrode during the local sheath collapse. This mechanism is illustrated in figure 19(b) by the arrow marked as ‘1’. Figure 17(b2) also shows some high energy  $\delta$ -electron bombardment of the powered electrode, which is absent in figure 17(a2). These  $\delta$ -electrons can only have such high energies, if they are emitted from an electrode at a time of high local sheath voltage, i.e. deeply inside the sheath. As shown in figure 19(b) by the arrows marked as ‘2’ and ‘3’, most of these  $\delta$ -electrons are induced by  $\gamma$ -electrons generated at the grounded electrode, which propagate towards the powered electrode, where they are reflected by the local sheath and propagate back towards the grounded electrode, where they arrive at the time the sheath has already started to expand. Thus, they hit the electrode and can generate  $\delta$ -electrons. In figure 18(b1), many electrons, indicated as ‘4’ arrive with high energy. These are electrons generated by ion induced ionization near the powered electrode. In addition, a green oblique line marked as ‘3’ appears at  $t/T_{\text{RF}} = 0.25$  in figure 18(b1) at energies up to about 300 eV. These are  $\gamma$ -electrons emitted at the grounded electrode, reflected by the sheath at the powered electrode and finally bombarding the grounded electrode, as shown in figure 19(b) by the red arrows marked as ‘3’.

The last column of figure 18 shows the results for case 4. In figure 18(c2), a large arc marked as ‘1, 2’ appears at  $t/T_{\text{RF}} = 0.5$ , which indicates that a number of electrons bombards the powered electrode with energies up to about 500 eV. According to figure 17(c2), most of these electrons are  $\gamma$ -electrons. Similar to the discussion of figure 18(b2),  $\gamma$ -electrons emitted at the grounded electrode can reach the powered electrode with energies up to 300 eV. Therefore, this high energy  $\gamma$ -electron bombardment of the powered electrode in figure 18(c2) is caused by  $\gamma$ -electrons emitted at the powered electrode. At  $t/T_{\text{RF}} = 0.5$ , the sheath is fully expanded at the powered electrode. As shown in figure 19(c) with arrows marked as ‘1’,  $\gamma$ -electrons emitted at the powered electrode at this time obtain very high energies and bombard the grounded electrode, where some of them are reflected and then penetrate into the sheath at the powered electrode. Upon arrival at the powered electrode, the local sheath has already started to collapse, i.e. a smaller voltage drops across it compared to the moment when the  $\gamma$ -electrons were generated at this electrode. Therefore, these  $\gamma$ -electrons can overcome the sheath voltage and bombard the powered electrode. With the increase of the sheath collapse velocity, the change of the sheath voltage during the transit time of these electrons through the bulk increases. As a result, the energy of the  $\gamma$ -electrons arriving at the powered electrode increases, as indicated by the rising

trend of the arc in figure 18(c2) during the time interval of  $t/T_{\text{RF}} = 0.55\text{--}0.87$ . From the time  $t/T_{\text{RF}} = 0.87$ , an electric field reversal appears, which makes the electrons bombard the electrode with even higher energies, as shown in figures 17(c2) and 18(c2).

In figure 17(c2), high energy  $\delta$ -electron bombardment at the powered electrode is also observed. These  $\delta$ -electrons are emitted at the powered electrode at the time of high instantaneous sheath voltage and are induced by high energy  $\gamma$ -electron bombardment based on the mechanism discussed before and as shown in figure 19(c) by the arrows marked as ‘2’. These emitted  $\delta$ -electrons are accelerated to high energies by the instantaneous sheath electric field at the powered electrode, propagate towards the grounded electrode, where some of them are reflected and return to the powered electrode, where they hit the surface around the time of local sheath collapse. In figure 18(c1), there are two large arcs with peak energies up to about 1.7 keV. The first arc is caused directly by the  $\gamma$ -electrons emitted at the powered electrode and the following arc is formed by  $\gamma$ -electrons that are initially reflected at the grounded electrode and propagate back towards the powered electrode, where they are again reflected by the sheath, move back to and bombard the electrode. This is illustrated in figure 19(c) by the arrows marked as ‘3’. Figure 17(c1) also shows high energy  $\delta$ -electron bombardment at the grounded electrode. These  $\delta$ -electrons are emitted at the powered electrode deep inside sheath, where they can be strongly accelerated and hit the grounded electrode at high energies, as indicated in figure 19(c) by the arrows marked as ‘2’.

In conclusion, these figures reveal the complicated electron dynamics in the presence of realistic SEE and show that secondary electrons do not only influence the plasma density, but also strongly affect the electron energy distributions at the boundary surfaces.

#### 4. Conclusions

The effects of the reactor geometry and of realistic energy as well as material dependent ion and electron induced SEECs on CCPs operated in argon at low pressure and high voltage were investigated based on 2D GPU accelerated PIC/MCC simulations. The radial uniformity of the space and time resolved electron dynamics was studied. Due to the high electron density near the reactor center, the ionization rate was found to be highest near the center region at most times within the RF period. During the sheath expansion phase, the simultaneous expansion of vertical and lateral sheaths close to the sidewalls at the electrode edge was found to cause the generation of energetic electron beams at the electrode edge, which propagate towards the reactor center and result in an ionization peak at the electrode edge. By increasing the geometrical asymmetry, a large DC self-bias is formed, which leads to the generation of a large sheath at the smaller powered electrode and induces significant changes to the electron dynamics. For asymmetric reactor geometries and during the sheath expansion phase, the plasma series resonance is self-excited. This

enhances the electron power absorption by generating several energetic electron beams during a single sheath expansion phase. During the sheath collapse phase, a strong electric field reversal establishes to compensate the ion flux to the electrode by electrons on time average in the presence strong secondary electron emission from this boundary surface. The reversed electric field was found to increase as a function of the geometric reactor asymmetry due to its effects on the sheath width. For the geometrically asymmetric cases a smaller sheath is formed at the grounded electrode, which reduces the electron power absorption on this side during the sheath expansion phase. This effect is the main reason for the reduced plasma density in the asymmetric discharges.

An analysis of the spatio-temporal ionization dynamics for different geometries revealed a strong effect of the reactor geometry and the electrode materials via the choice of the SEECs in the simulation. Electron induced secondary electrons, i.e.  $\delta$ -electrons, are found to cause up to 51% of the total ionization directly. Ion induced secondary electrons, i.e.  $\gamma$ -electrons, were found not to contribute much to the ionization directly at these low pressure conditions, because they are too energetic after being accelerated in the sheath. However, they are very important for the generation of  $\delta$ -electrons at boundary surfaces. Especially in asymmetric discharges,  $\gamma$ -electrons are the major source for  $\delta$ -electron emission at the grounded electrode, where they can overcome the local sheath potential and bombard the electrode at high energies after being accelerated by the sheath electric field at the opposite electrode. The electron and ion energy distribution functions at the electrodes were also found to be affected by the reactor geometry. Very high energy ion bombardment at the powered electrode, and high energy  $\gamma$ -electron bombardment at the grounded electrode are observed in the asymmetric discharges.

To clarify the physical mechanisms behind the formation of the EFEDFs at the electrodes, the effects of individual surface coefficients on the discharge were investigated by changing the surface coefficients at the electrodes systematically. Including only  $\gamma$ - or  $\delta$ -electrons in the simulation leads to a similar increase of the plasma density compared to simulations, where both SEECs are neglected. If both SEECs are included, a much stronger increase of the plasma density is found, i.e. there is a synergistic effect related to the generation of  $\delta$ -electrons by  $\gamma$ -electrons. Stronger electron emission from the boundary surfaces is also found to lead to the generation of stronger electric field reversal during the sheath collapse at the powered electrode, since the SEE reduces the effective electron flux to the electrode and a stronger field reversal is required to accelerate electrons towards the electrode to compensate the ion flux on time average. The total ionization rate is enhanced, if both  $\gamma$ - and  $\delta$ -electron emission are included, especially during the sheath collapse at the grounded electrode, because ionization caused by  $\delta$ -electrons is important at this time within the RF period and the  $\delta$ -electron density is highest in this case. The strong ionization caused by these  $\delta$ -electrons leads to a higher plasma density.

Finally, the energy distributions of various electron species at the electrodes were analyzed for different surface conditions. The EFEDF shapes were found to be caused by complex

electron dynamics, including reflections of  $\delta$ - and  $\gamma$ -electrons from boundary sheaths and surfaces.

Our results show that the geometrical reactor asymmetry strongly influences the plasma density and can induce significant changes of the charged particle dynamics and their distribution functions. Electron and ion induced secondary electrons were found to play an important role at the low pressure conditions studied in this work. Therefore, they need to be taken into account realistically in the simulations. In addition to their fundamental relevance, the results obtained are important for applications, where they can serve as a basis for plasma reactor design and knowledge based process development. Clearly, additional investigations of more complex gases are required in the future.

## Acknowledgments

This work was supported by the German Research Foundation in the frame of the project 'Electron heating in capacitive RF plasmas based on moments of the Boltzmann equation: from fundamental understanding to knowledge based process control' (No. 428942393) and within the frame of the collaborative research centre SFB-TR 87 (project C1), by the National Office for Research, Development and Innovation of Hungary (NKFIH) via the grant 134462, by the National Natural Science Foundation of China (Grant No. 12020101005, 11975067), and by the China Scholarship Council (No. 201906060024).

## Data availability statement

The data that support the findings of this study are available upon reasonable request from the authors.

## ORCID iDs

Li Wang  <https://orcid.org/0000-0002-3106-2779>  
 Peter Hartmann  <https://orcid.org/0000-0003-3572-1310>  
 Zoltán Donkó  <https://orcid.org/0000-0003-1369-6150>  
 Yuan-Hong Song  <https://orcid.org/0000-0001-5712-9241>  
 Julian Schulze  <https://orcid.org/0000-0001-7929-5734>

## References

- [1] Lieberman M A and Lichtenberg A J 2005 *Principles of Plasma Discharges and Materials Processing* 2nd edn (New York: Wiley)
- [2] Chabert P and Braithwaite N 2011 *Physics of Radio-Frequency Plasmas* (Cambridge: Cambridge University Press)
- [3] Makabe T and Petrovic Z L 2014 *Plasma Electronics: Applications in Microelectronic Device Fabrication* 2nd edn (Boca Raton, FL: CRC Press)
- [4] Huang S, Huard C, Shim S, Nam S K, Song I-C, Lu S and Kushner M J 2019 *J. Vac. Sci. Technol. A* **37** 031304
- [5] Huang S, Shim S, Nam S K and Kushner M J 2020 *J. Vac. Sci. Technol. A* **38** 023001
- [6] Olevanov M, Proshina O, Rakhimova T and Voloshin D 2008 *Phys. Rev. E* **78** 026404
- [7] Köhler K, Coburn J W, Horne D E, Kay E and Keller J H 1985 *J. Appl. Phys.* **57** 59–66

- [8] Sansonnens L, Howling A A and Hollenstein C 2006 *Plasma Sources Sci. Technol.* **15** 302–13
- [9] Schulze J, Schüngel E, Czarnetzki U, Gebhardt M, Brinkmann R P and Mussenbrock T 2011 *Appl. Phys. Lett.* **98** 031501
- [10] Zhang Q-Z, Zhao S-X, Jiang W and Wang Y-N 2012 *J. Phys. D: Appl. Phys.* **45** 305203
- [11] Takao Y, Matsuoka K, Eriguchi K and Ono K 2011 *Jpn. J. Appl. Phys.* **50** 08JC02
- [12] Alexandrov A L and Schweigert I V 2005 *Plasma Sources Sci. Technol.* **14** 209–18
- [13] Hartmann P et al 2020 *Plasma Sources Sci. Technol.* **29** 075014
- [14] Wilczek S, Trieschmann J, Schulze J, Schuengel E, Brinkmann R P, Derzsi A, Korolov I, Donkó Z and Mussenbrock T 2015 *Plasma Sources Sci. Technol.* **24** 024002
- [15] Donkó Z, Schulze J, Czarnetzki U and Luggenhölscher D 2009 *Appl. Phys. Lett.* **94** 131501
- [16] Mussenbrock T, Brinkmann R P, Lieberman M A, Lichtenberg A J and Kawamura E 2008 *Phys. Rev. Lett.* **101** 085004
- [17] Czarnetzki U, Mussenbrock T and Brinkmann R P 2006 *Phys. Plasmas* **13** 123503
- [18] Horváth B, Daksha M, Korolov I, Derzsi A and Schulze J 2017 *Plasma Sources Sci. Technol.* **26** 124001
- [19] Horváth B, Schulze J, Donkó Z and Derzsi A 2018 *J. Phys. D: Appl. Phys.* **51** 355204
- [20] Greb A, Niemi K, O'Connell D and Gans T 2013 *Appl. Phys. Lett.* **103** 244101
- [21] Gudmundsson J T and Lieberman M A 2015 *Plasma Sources Sci. Technol.* **24** 035016
- [22] Proto A and Gudmundsson J T 2018 *Plasma Sources Sci. Technol.* **27** 074002
- [23] Lafleur T, Schulze J and Donkó Z 2019 *Plasma Sources Sci. Technol.* **28** 040201
- [24] Takagi S, Chikata T and Sekine M 2020 *Japan. J. Appl. Phys.* **60** SAAB07
- [25] Rauf S, Bera K and Collins K 2009 *Plasma Sources Sci. Technol.* **19** 015014
- [26] Donkó Z, Schulze J, Hartmann P, Korolov I, Czarnetzki U and Schüngel E 2010 *Appl. Phys. Lett.* **97** 081501
- [27] Küllig C, Dittmann K, Wegner T, Sheykin I, Matyash K, Loffhagen D, Schneider R and Meichsner J 2012 *Contrib. Plasma Phys.* **52** 836
- [28] Schulze J, Derzsi A, Dittmann K, Hemke T, Meichsner J and Donkó Z 2011 *Phys. Rev. Lett.* **107** 275001
- [29] Sun G Y, Li H W, Sun A B, Li Y, Song B P, Mu H B, Li X R and Zhang G J 2019 *Plasma Process. Polym.* **16** 1900093
- [30] Wang L, Wen D-Q, Zhang Q-Z, Song Y-H, Zhang Y-R and Wang Y-N 2019 *Plasma Sources Sci. Technol.* **28** 055007
- [31] Liu G-H, Wang X-Y, Liu Y-X, Sun J-Y and Wang Y-N 2018 *Plasma Sources Sci. Technol.* **27** 064004
- [32] Proto A and Gudmundsson J T 2018 *Atoms* **6** 65
- [33] Rakhimova T V et al 2006 *IEEE Trans. Plasma Sci.* **34** 867–77
- [34] Belenguer P and Boeuf J P 1990 *Phys. Rev. A* **41** 4447–59
- [35] Schulze J, Heil B G, Luggenhölscher D and Czarnetzki U 2008 *IEEE Trans. Plasma Sci.* **36** 1400–1
- [36] Schulze J, Kampschulte T, Luggenhölscher D and Czarnetzki U 2007 *J. Phys.: Conf. Ser.* **86** 012010
- [37] Booth J P, Curley G, Marić D and Chabert P 2009 *Plasma Sources Sci. Technol.* **19** 015005
- [38] Zhang Q-Z, Wang Y-N and Bogaerts A 2014 *J. Appl. Phys.* **115** 223302
- [39] Schulze J, Donkó Z, Schüngel E and Czarnetzki U 2011 *Plasma Sources Sci. Technol.* **20** 045007
- [40] Lafleur T, Chabert P and Booth J P 2013 *J. Phys. D: Appl. Phys.* **46** 135201
- [41] Korolov I, Derzsi A, Donkó Z and Schulze J 2013 *Appl. Phys. Lett.* **103** 064102
- [42] Derzsi A, Korolov I, Schüngel E, Donkó Z and Schulze J 2015 *Plasma Sources Sci. Technol.* **24** 034002
- [43] Daksha M, Derzsi A, Wilczek S, Trieschmann J, Mussenbrock T, Awakowicz P, Donkó Z and Schulze J 2017 *Plasma Sources Sci. Technol.* **26** 085006
- [44] Daksha M, Derzsi A, Mujahid Z, Schulenberg D, Berger B, Donkó Z and Schulze J 2019 *Plasma Sources Sci. Technol.* **28** 034002
- [45] Hannesdottir H and Gudmundsson J T 2016 *Plasma Sources Sci. Technol.* **25** 055002
- [46] Sun J-Y, Wen D-Q, Zhang Q-Z, Liu Y-X and Wang Y-N 2019 *Phys. Plasmas* **26** 063505
- [47] Braginsky O, Kovalev A, Lopaev D, Proshina O, Rakhimova T, Vasilieva A, Voloshin D and Zyryanov S 2012 *J. Phys. D: Appl. Phys.* **45** 015201
- [48] Derzsi A, Horváth B, Donkó Z and Schulze J 2020 *Plasma Sources Sci. Technol.* **29** 074001
- [49] Wen D-Q, Kawamura E, Lieberman M A, Lichtenberg A J and Wang Y-N 2017 *Phys. Plasmas* **24** 083517
- [50] Liu Y, Booth J-P and Chabert P 2018 *Plasma Sources Sci. Technol.* **27** 025006
- [51] Zhang Y-R, Xu X, Zhao S-X, Bogaerts A and Wang Y-N 2010 *Phys. Plasmas* **17** 113512
- [52] Bera K, Rauf S, Balakrishna A and Collins K 2010 *IEEE Trans. Plasma Sci.* **38** 3241–8
- [53] Bera K, Rauf S, Ramaswamy K and Collins K 2009 *J. Vac. Sci. Technol. A* **27** 706–11
- [54] Zhao K, Wen D Q, Liu Y X, Lieberman M A, Economou D J and Wang Y N 2019 *Phys. Rev. Lett.* **122** 185002
- [55] Liu Y-X, Liang Y-S, Wen D-Q, Bi Z-H and Wang Y-N 2015 *Plasma Sources Sci. Technol.* **24** 025013
- [56] Perret A, Chabert P, Jolly J and Booth J-P 2005 *Appl. Phys. Lett.* **86** 021501
- [57] Eremin D, Bienholz S, Szeremley D, Trieschmann J, Ries S, Awakowicz P, Mussenbrock T and Brinkmann R P 2016 *Plasma Sources Sci. Technol.* **25** 025020
- [58] Wen D-Q, Kawamura E, Lieberman M A, Lichtenberg A J and Wang Y-N 2017 *J. Phys. D: Appl. Phys.* **50** 495201
- [59] Sansonnens L and Schmitt J 2003 *Appl. Phys. Lett.* **82** 182–4
- [60] Chabert P, Raimbault J-L, Rax J-M and Perret A 2004 *Phys. Plasmas* **11** 4081–7
- [61] Rauf S and Balakrishna A 2017 *J. Vac. Sci. Technol. A* **35** 021308
- [62] Schmidt H, Sansonnens L, Howling A A, Hollenstein C, Elyakoubi M and Schmitt J P M 2004 *J. Appl. Phys.* **95** 4559–64
- [63] Ohtsu Y, Matsumoto N, Schulze J and Schuengel E 2016 *Phys. Plasmas* **23** 033510
- [64] Overzet L J and Hopkins M B 1993 *Appl. Phys. Lett.* **63** 2484–6
- [65] Jeon B, Chang H-Y, Song J-K and Jeon C-W 2002 *Plasma Sources Sci. Technol.* **11** 520–4
- [66] Babaeva N Y and Kushner M J 2007 *J. Appl. Phys.* **101** 113307
- [67] Rauf Shahid 2020 *Plasma Sources Sci. Technol.* **29** 095019
- [68] Lieberman M A, Booth J P, Chabert P, Rax J M and Turner M M 2002 *Plasma Sources Sci. Technol.* **11** 283–93
- [69] Wen D-Q, Kawamura E, Lieberman M A, Lichtenberg A J and Wang Y-N 2016 *Plasma Sources Sci. Technol.* **26** 015007
- [70] Mussenbrock T, Hemke T, Ziegler D, Brinkmann R P and Klick M 2008 *Plasma Sources Sci. Technol.* **17** 025018
- [71] Ries S, Banko L, Hans M, Primetzhofer D, Schneider J M, Ludwig A, Awakowicz P and Schulze J 2019 *Plasma Sources Sci. Technol.* **28** 114001
- [72] Hegemann D, Michlíček M, Blanchard N E, Schütz U, Lohmann D, Vandenbossche M, Zajíčková L and Drábik M 2016 *Plasma Process. Polym.* **13** 279–86
- [73] Hegemann D, Bülbül E, Hanselmann B, Schütz U, Amberg M and Gaiser S 2020 *Plasma Processes Polym.* **n/a** e2000176

- [74] Konstantinidis E and Cotronis Y 2012 Accelerating the red/black SOR method using GPUs with CUDA *Parallel Processing and Applied Mathematics* ed R Wyrzykowski, J Dongarra, K Karczewski and J Waśniewski (Berlin: Springer) pp 589–98
- [75] Evans D 1984 *Parallel Comp.* **1** 3–18
- [76] COP database [www.lxcat.net](http://www.lxcat.net) retrieved on January 10, 2020
- [77] McEachran R and Stauffer A 2014 *Eur. Phys. J. D* **68** 153
- [78] Hayashi database [www.lxcat.net](http://www.lxcat.net) retrieved on January 10, 2020
- [79] Hayashi M 2003 Bibliography of electron and photon cross sections with atoms and molecules published in the 20th century - argon *Technical Report NIFS-DATA-072* (Toki, Gifu, Japan: National Institute for Fusion Science) pp 509-5292 [www.nifs.ac.jp/report/NIFS-DATA-072.pdf](http://www.nifs.ac.jp/report/NIFS-DATA-072.pdf)
- [80] Phelps A V 1991 *J. Phys. Chem. Ref. Data* **20** 557–73
- [81] Phelps A V 1994 *J. Appl. Phys.* **76** 747–53
- [82] Donkó Z 2011 *Plasma Sources Sci. Technol.* **20** 024001
- [83] Donkó Z 1998 *Phys. Rev. E* **57** 7126–37
- [84] Okhrimovskyy A, Bogaerts A and Gijbels R 2002 *Phys. Rev. E* **65** 037402
- [85] Phelps A V and Petrovic Z L 1999 *Plasma Sources Sci. Technol.* **8** R21–44
- [86] Sobolewski M 2020 *73rd Annual Gaseous Electronics Conference 62 BAPS.2017.GEC.WF2.2* <http://meetings.aps.org/link/BAPS.2017.GEC.WF2.2>
- [87] Dunning F B, Smith A C H and Stebbings R F 1971 *J. Phys. B: At. Mol. Phys.* **4** 1683–95
- [88] Dunning F B and Smith A C H 1971 *J. Phys. B: At. Mol. Phys.* **4** 1696–710
- [89] Donkó Z, Schulze J, Heil B G and Czarnetzki U 2008 *J. Phys. D: Appl. Phys.* **42** 025205
- [90] Schmidt N, Schulze J, Schüngel E and Czarnetzki U 2013 *J. Phys. D: Appl. Phys.* **46** 505202
- [91] Wilczek S et al 2016 *Phys. Plasmas* **23** 063514
- [92] Sato A H and Lieberman M A 1990 *J. Appl. Phys.* **68** 6117–24
- [93] Vender D and Boswell R W 1992 *J. Vac. Sci. Technol. A* **10** 1331–8
- [94] Campanell M D, Khrabov A V and Kaganovich I D 2012 *Phys. Rev. Lett.* **108** 255001
- [95] Campanell M D 2013 *Phys. Rev. E* **88** 033103
- [96] Wild C and Koidl P 1991 *J. Appl. Phys.* **69** 2909–22
- [97] Fu Y, Zheng B, Wen D-Q, Zhang P, Fan Q H and Verboncoeur J P 2020 *Plasma Sources Sci. Technol.* **29** 09LT01
- [98] Vass M, Derzsi A, Schulze J and Donko Z 2021 Electron tennis driven by radio-frequency electric fields in low-pressure plasma sources *Plasma Sources Sci. Technol.* **30** 03LT04